ADVANCED SUSTAINABLE SYSTEMS
www.advsustainsys.com

# Electro-Conductive Silver-Coated Polyamide-Imide Membranes for Sustainable Water Treatment

*Zahra Zandi, Mehrasa Yassari, Mojtaba Mohseni, Hesam Jafarian, Mohsen Pilevar, Mahshid Mardani, Farah Rahman Omi, Mark Elliott, Ahmad Rahimpour, Matthias Wessling, Mostafa Dadashi Firouzjaei,* and Mohtada Sadrzadeh**

**This study focuses on developing and evaluating electro-conductive polyamide-imide (PAI) ultrafiltration membranes with a stable metallic coating that can tackle the dual challenges of dye removal and membrane fouling in wastewater treatment applications. The Ag-coated PAI membranes exhibit high electrical conductivity (exceeding $5.6 \times 10^4$ S cm$^{-1}$), enabling the use of an applied electric potential to enhance dye removal efficiency and mitigate membrane fouling via electrochemical mechanisms. The electrochemical impedance spectroscopy (EIS) test confirm the high conductivity of the membranes. Meanwhile, linear sweep voltammetry (LSV) revealed the presence of the oxygen reduction reaction (ORR) and the hydrogen evolution reaction (HER) on the membrane surface. These findings provide valuable insights into the electrochemical potential for fabricating electro-conductive membranes (ECMs). The Ag-PAI membranes demonstrate remarkable dye rejection, with rates reaching 97% for reactive red 120 (RR120) and 90% for reactive black (RB) at an applied voltage of 7 V, while maintaining a consistent permeate flux of ≈100 LMH. The membranes also show significantly improved resistance to organic fouling, with the flux recovery ratio (FRR) increasing from 49.14% for pristine PAI to 80.41%, representing a 31% enhancement. The enhanced antifouling performance is attributed to gas bubble formation during voltage application, which disrupted the accumulation of the fouling cake layer. Together, these mechanisms effectively enhance the overall performance of the membrane.**

## 1. Introduction

Membrane fouling, particularly biofouling, is a major obstacle limiting the long-term efficiency of water treatment processes. Biofouling accounts for the largest share of total fouling and can increase operational costs by 30% to 50%.[1–3] Despite advantages such as energy efficiency, simple operation, and compact design,[4,5] membrane systems remain susceptible to fouling, which significantly reduces their performance.[6,7]

To mitigate fouling, various strategies have been explored, including surface modifications and the development of membranes responsive to external stimuli such as temperature,[8,9] pH,[10,11] magnetic fields,[12,13] and electric fields.[14,15] The latter is among the most recent advances in membrane technology, offering easy implementation and precise control within the membrane process.[16,17] An electric field initiates electrochemical reactions that dislodge foulants and dyes, enhance mass transfer, and reduce membrane fouling.[18]

Z. Zandi, M. Yassari, F. R. Omi, A. Rahimpour, M. Dadashi Firouzjaei, M. Sadrzadeh
Department of Mechanical Engineering
10-367 Donadeo Innovation Center for Engineering
Advanced Water Research Lab (AWRL)
University of Alberta
Edmonton, AB T6G 1H9, Canada
E-mail: mdfirouzjaei@ua.edu; sadrzadeh@ualberta.ca

The ORCID identification number(s) for the author(s) of this article can be found under https://doi.org/10.1002/adsu.202500527



**DOI: 10.1002/adsu.202500527**

M. Mohseni, M. Wessling
Chemical Process Engineering AVT.CVT
RWTH Aachen University
Forckenbeckstr. 51, 52074 Aachen, Germany

H. Jafarian, M. Pilevar, M. Mardani, M. Elliott, M. Dadashi Firouzjaei
Department of Civil
Construction
and Environmental Engineering
University of Alabama
Tuscaloosa, AL 35487, USA

M. Wessling
DWI Leibniz Institute for Interactive Materials
Forckenbeckstr. 50, 52074 Aachen, Germany

The key mechanisms involved include electrophoresis, electroosmosis, electrostatic repulsion, and electrochemical reactions, all occurring at the surface of electro-conductive membranes (ECM).[19–24] The applied electric field drives ion migration through the solution (electrophoresis), which can oppose the convective transport of charged species toward the membrane surface and reduce their accumulation.[25,26] This ion movement can also generate fluid convection within small pores (electroosmosis), further improving mass transport.[27,28] Electrostatic repulsion occurs when the membrane surface carries the same charge as the foulants, effectively repelling them and limiting surface accumulation.[28]

The electrochemical reactions on ECM surfaces can degrade pollutants directly at the membrane surface. These reactions include oxidation processes that generate reactive species such as hydroxyl radicals ($OH^{\bullet}$),[29] direct electron transfer reactions,[30] and hydrogen peroxide ($H_2O_2$) generation via oxygen reduction in Fenton reactions[31] at the membrane surface. Applying a more negative potential and creating higher potential differences in electrochemical systems generates hydrogen ($H_2$) and oxygen ($O_2$) bubbles. These bubbles repel attached foulants away from the membrane surface, further improving the antifouling performance.[32,33] Therefore, ECMs simultaneously mitigate fouling and degrade pollutants in situ, making them practical for water treatment.[19,20]

To maximize the potential of the electrified membrane systems, various electro-conductive materials, including carbon nanotubes (CNTs),[34,35] graphene,[20] MXene,[36,37] and metal-based coatings[38–42] have been used for ECM fabrication. These materials impart conductivity, enabling the membranes to act as porous electrodes in a two-electrode setup with working and counter electrodes. However, despite the effectiveness of electrochemical reactions and electrostatic forces in fouling mitigation, some microorganisms may still form biofilms on the membrane.[43] This limitation is largely due to the insufficient gas bubble formation during water electrolysis, which reduces the effectiveness of cell detachment from the membrane surface.[44] Integrating conductive materials with antibacterial properties may be a promising solution to address this issue.

Silver stands out for its high electrical conductivity ($0.063 \times 10^7$ S $cm^{-1}$)[45] and antimicrobial properties, making it increasingly popular in developing ECMs for water treatment.[46,47] The incorporation of silver nanoparticles (Ag-NPs) into membranes boosts their antibacterial effectiveness through two mechanisms: the controlled release of highly reactive silver ions ($Ag^+$), which can disrupt bacterial cells and damage their membranes, and the production of reactive oxygen species that target and degrade bacterial structures.[46] The antibacterial activity of silver is well-established, relying on the interaction of $Ag^+$ with electron donor groups in biological materials containing oxygen, nitrogen, or sulfur.[48] However, excessive or uncontrolled release of silver nanoparticles can lead to diminished long-term antibacterial performance and potential environmental concerns. Recent studies have explored methods to control silver release in membranes, particularly through the fabrication of silver-based metal-organic framework (AgMOF) membranes, as the organic framework serves as a barrier to metal leaching.[49,50] Techniques such as in situ surface functionalization of polyamide thin-film composite (TFC) membranes with AgMOFs [51] or integrating Ag-MOFs during interfacial polymerization (IP) [52] have successfully regulated silver release. In parallel, several techniques have been developed to incorporate silver into membranes, including in situ reduction, complex surface modifications using polydopamine, and electrospinning.[53–57] Beyond these, other metal deposition techniques, such as arc plasma deposition and electroless plating, have been used to fabricate silver-functionalized membranes. Arc plasma deposition provides robust immobilization of AgNPs with proven antibacterial performance; however, it requires expensive vacuum systems and complex equipment, which limits scalability.[58] Similarly, electroless deposition can produce electro-conductive surfaces, but the process involves multiple steps, chemical activation, and is primarily applied to metallic or rigid supports rather than polymeric filtration membranes.[59,60]

While these approaches have demonstrated improved antibacterial performance, they often suffer from limitations, including increased fabrication complexity and cost, limited scalability for large-scale membrane production, and poor stability due to silver nanoparticle leaching. Moreover, these methods typically fail to fully exploit the electro-conductive and antibacterial properties of silver in membranes simultaneously. Therefore, to overcome these limitations, it is essential to employ methods that ensure a stable and uniform silver layer on the membrane surface, effectively utilizing both its antibacterial properties and electro-conductivity to enhance performance and longevity.[61,62]

As a promising alternative, the spray-coating technique has shown significant potential. Various spraying methods, including cold spray, blow spray, and plasma spray, have been explored for silver coatings.[63–65] However, their application to porous membranes for water treatment remains limited. Cold spray, for instance, suffers from poor control over coating uniformity and thickness, while plasma-based methods require high-cost equipment, limiting their scalability for membrane fabrication. The spray-coating technique rapidly atomizes the silver nanoparticle suspension, allowing for the uniform formation of a surface layer while minimizing nanoparticle penetration into the membrane support. Rapid droplet drying reduces nanoparticle intrusion into the porous substrate,[66,67] while the fine droplet size and enhanced spreading improve surface wetting and strengthen the interaction between silver nanoparticles and the membrane matrix, enhancing coating stability.[68]

In this study, for the first time, a simple, low-pressure technique was applied to deposit a homogeneous and electro-conductive layer of silver nanoparticles onto the polyamide-imide (PAI) ultrafiltration (UF) membranes. Unlike previously reported silver nanoparticle membrane modification methods, this approach provides a straightforward, scalable coating process without the need for complex plasma systems, high temperatures, or vacuum equipment. Simultaneously, it enhances both the antibacterial performance and electro-conductivity of the membranes, enabling active fouling mitigation and long-term operational stability. The robust silver coating imparts electrical conductivity to the PAI membranes, allowing the application of an electric potential that enhances dye rejection and reduces fouling through electrochemical reactions. Additionally, the antimicrobial properties of the membranes were evaluated to assess their potential for use in anti-biofouling applications. Finally, the stability of the silver coating was thoroughly assessed under

various operational conditions to confirm its durability. Our findings demonstrate that these silver-coated PAI membranes provide a sustainable solution for contaminant removal and fouling mitigation, contributing to more efficient water treatment processes.

## 2. Materials and Methods

### 2.1. Chemicals and Reagents

Aqueous silver nanoparticle solution with 52% silver loading (SPI 508) was purchased from Novacentrix company (USA). N, N-dimethylacetamide (DMAc, >99.9%), calcium chloride ($CaCl_2$), sulfuric acid ($H_2SO_4$), and acetone were provided by Fisher Scientific. Hydrochloric acid (HCl) was supplied by Anachemica. Polyvinylpyrrolidone (PVP, 360 kDa), poly (ethylene glycol) (PEG, 2kDa), sodium alginate (SA), glacial acetic acid (ReagentPlus, 99.0%), and sodium hydroxide (NaOH) were purchased from Sigma-Aldrich. Sodium sulfate ($Na_2SO_4$) and oxygen ($O_2$), with a purity of 99.995 %, were supplied by Sigma Aldrich and Nippon gases, respectively. Trypticase soy broth (TSB), agar, phosphate buffer saline (PBS), and *Escherichia coli* (*E. coli*, ATCC 35695), as a gram-negative model bacterium, were used in antibacterial tests. Polyamide-imide (PAI, Torlon 4000 THV) was supplied by Solvay Advanced Polymers. Reactive Red 120 (RR120, MW: 1774.15 Da) and reactive black (RB, MW: 991.82 Da) dyes were acquired from Sigma-Aldrich and utilized as organic contaminants for dye removal experiments. Deionized water (DI) was used for all experiments throughout this research.

### 2.2. Fabrication of the PAI Support Layer

The PAI support layers were fabricated using the non-solvent-induced phase separation (NIPS) technique. PAI, specifically Torlon 4000 THV, was chosen for its outstanding thermal, mechanical, and chemical resistance and remarkable hydrophilicity. DMAc served as the solvent throughout the procedure. A uniform polymer solution was prepared by dissolving 9 wt.% PAI in DMAc, followed by stirring at 350 rpm and maintaining the temperature at 45 °C for 24 h. The homogenous solution was then allowed to rest in a vacuum oven for 10 min to eliminate any trapped air bubbles.

Finally, the large-scale membrane fabrication casting device prepared the PAI support layer using a film applicator to cast the solution onto a non-woven polyester fabric. Lastly, the cast film was immersed in a coagulation bath containing deionized water, where it remained overnight to ensure the complete removal of the solvent from the polymer matrix.

### 2.3. Electro-Conductive Ag-PAI Membrane Fabrication

Following PAI membrane fabrication, an Ag-coated PAI membrane was prepared using a facile spray coating method. This approach utilized an airbrush equipped with a 1 mm diameter nozzle to spray the Ag ink under an air pressure of 25 psi. During spraying, 3 mL of silver ink was evenly distributed onto the PAI membrane with a surface area of 1000 $cm^2$. A constant distance of 25 cm was maintained between the membrane and the airbrush to ensure uniform coverage and prevent the formation of large silver droplets. After applying the silver ink on top of the PAI membrane surface, the coated membrane underwent a curing step to ensure the adhesion and stability of the silver coating onto the PAI membrane surface. In this curing process, the membrane was cured in an oven at 80 °C for 20 min. The membrane was then cooled down to room temperature, completing the fabrication process of the electro-conductive Ag-PAI membrane. **Figure 1** presents a schematic illustration of the Ag-PAI membrane fabrication process, highlighting key stages from initial preparation to final ECM formation.

Employing commercially available silver nanoparticles on the membrane surface and curing the coated membrane provided a straightforward and effective approach for preparing the PAI membrane with a conductive silver coating layer. This process resulted in the fabrication of Ag-PAI membranes with electro-conductive properties, making them suitable for various applications. These membranes demonstrate potential as practical solutions in water treatment, particularly with membrane-based technologies that utilize electrochemical assistance. Accordingly, the prepared Ag-PAI membranes were further evaluated for their electrochemical performance, antifouling behavior, and dye removal efficiency in the subsequent sections.

### 2.4. Characterizations of Silver Nanoparticles

The chemical composition of silver nanoparticles was analyzed by X-ray photoelectron spectroscopy (XPS, Kratos AXIS ULTRA), equipped with a monochromatic Al K$\alpha$ X-ray source operating at 1496 eV. Dynamic light scattering (DLS) with an ALV/CGS-3 Goniometer was employed to assess the size distribution and hydrodynamic radius using photon correlation spectroscopy. Before measurement, the silver nanoparticle sample was diluted in DI water and sonicated for 10 min. Morphological analysis was performed using field emission scanning electron microscopy (FE-SEM, Zeiss Sigma 300 VP) with an integrated energy dispersive X-ray (EDX) spectrometer, as well as transmission electron microscopy (TEM, Philips/FEI Morgagni 268). The crystalline structure of silver nanoparticles was analyzed using X-ray diffraction (XRD) with a 2$\theta$ range of 20° to 90°, utilizing a Bruker D8 Advance diffractometer. The X-ray source was a cobalt anode, with copper as the background material.

### 2.5. Characterizations of the Fabricated Membranes

The surface wettability of both pristine PAI membrane and Ag-PAI membrane was evaluated by measuring the water contact angles (WCA) utilizing a drop shape analyzer (DSA 100E, KRÜSS GmbH, Germany). WCA was measured at five different positions on the surface for both samples, and the average value was reported. The pristine PAI membrane and Ag-PAI membrane morphology were analyzed using field-emission SEM (FE-SEM) equipped with an EDX spectrometer. The surface zeta potential of the membranes was measured using a Surpass 3 electrokinetic analyzer (Anton Paar, Graz, Austria). Zeta potential values were

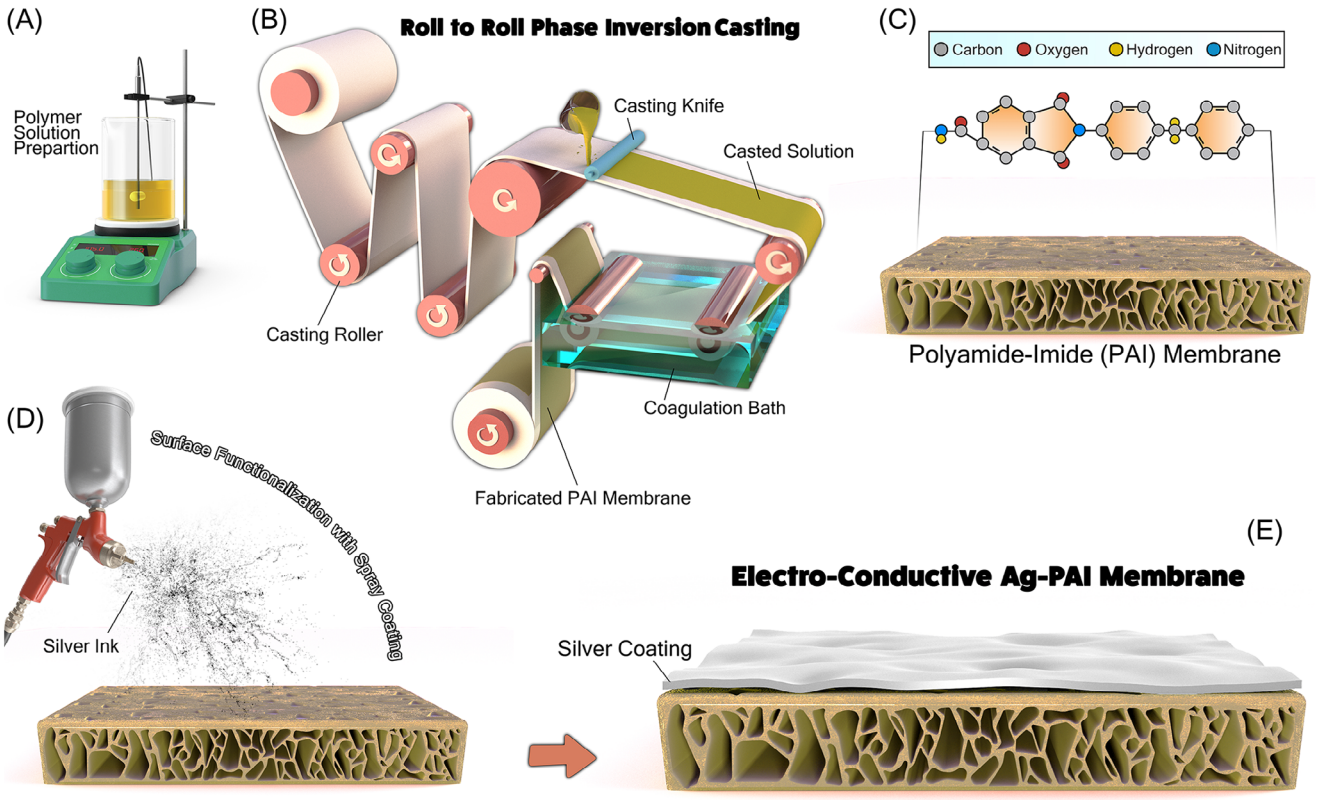


**Figure 1.** Schematic illustration of the step-by-step fabrication process of electro-conductive Ag-PAI membranes.

evaluated across a pH range of 4–9 at 25 °C, using a 1 mM KCl solution based on streaming potential measurements. The pH of the electrolyte solution was adjusted to the target level using HCl and NaOH solutions to facilitate analysis. The charge properties of the membranes were analyzed further using the ion elution method, which quantified the density of carboxylic groups present within the pores of the pristine PAI and modified PAI membranes. This analysis used inductively coupled plasma mass spectrometry (ICP-MS; 143 NEXION 300D, PerkinElmer). Full details of all characterization protocols are provided in Sections S1–S3 (Supporting Information).

The molecular weight cut-off (MWCO) of the membrane was evaluated by filtering a polyethylene glycol (PEG) solution with a total concentration of 200 ppm and molecular weights ranging from 200 to 8000 Da. The PEG solution was filtered for 1 h at a pressure of 20 psi, and the concentration of PEG in the permeate was measured using total organic carbon (TOC) analysis with a Shimadzu TOC-L instrument. The Stokes radius ($r_s$) of the Ag-PAI membrane was calculated using Equation S1 of Section S4 (Supporting Information), which defines the molecular weight (MW) of PEG at a rejection rate of 90%.[69] The relationship between the pore size distribution of a membrane and the Stokes radius of a neutral solute is defined in Equation S2 in Section S4 (Supporting Information).

The surface electrical resistivity of the membranes was measured using a four-point probe resistivity measurement device (PRO4-4000) connected to a Keithley 2601A power source meter (Section S5, Supporting Information).

The linear sweep voltammetry (LSV) experiments were conducted in an undivided flow-through module using our standard electrochemical cell (Flex-E-Cell, Flex-X-cell GmbH). An expanded metal titanium sheet coated with platinum (Magneto), measuring 4.5 × 5.0 $cm^2$, the synthesized Ag-PAI membrane (1.5 × 3 $cm^2$), and a potassium-saturated $Hg_2SO_4$ (0.64 V vs. the standard hydrogen electrode (SHE)) served as the counter, working, and reference electrodes, respectively. A 100 mL solution of 50 mM $Na_2SO_4$ at pH 3 ± 0.1 was circulated through the module at a 50 mL $min^{-1}$ flow rate as the background electrolyte. During LSV measurements, the electrolyte was continuously bubbled with $N_2$ and $O_2$ gases, starting 10 min before the experiment to ensure complete saturation. $N_2$ bubbling was performed to remove dissolved oxygen and prevent re-entry of atmospheric oxygen, while $O_2$ bubbling was applied to achieve oxygen-saturated conditions for ORR evaluation.[70,71]

The electrochemical impedance spectroscopy (EIS) experiments were also performed in the cell before the LSV measurements at open-circuit potential, covering frequencies ranging from 0.1 Hz to 100 kHz. **Figure 2** displays the schematic of the experimental setups for both undivided and divided cells. To analyze the electro-generation of hydrogen peroxide ($H_2O_2$), chrono-amperometry (CA) experiments were carried out in the same flow-through module but divided into two compartments using a cation exchange membrane (Nafion 117) to avoid possible oxidation of formed $H_2O_2$ on the anode surface. Similar to LSV experiments, 50 mM $Na_2SO_4$ at pH 3 ± 0.1 was circulated as catholyte, but at a reduced volume of 50 mL to increase the

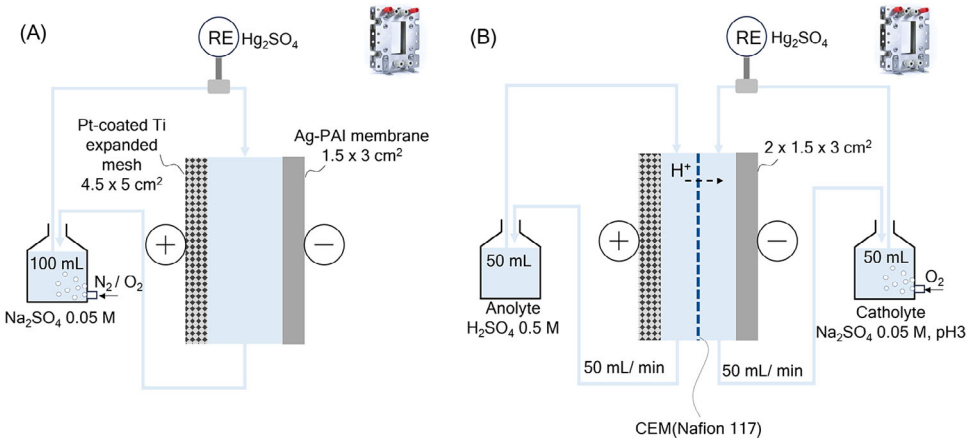


**Figure 2.** The schematic of the experimental setup used in LSV, CA, and multi-chrono-amperometry (MCA) experiments for A) undivided and B) divided cell configurations in a flow-through module.

concentration of $H_2O_2$ for improved detection precision. Additionally, the geometrical surface of Ag-PAI membranes was doubled to 9 $cm^2$. In the anode compartment, 50 mL of 500 mM $H_2SO_4$ solution was circulated as the anolyte. A distance of 3 mm was considered between the counter and the working electrode. During CA experiments, 1 mL samples of catholyte were collected at predefined time intervals for $H_2O_2$ measurement using a colorimetric method at 450 nm through a reaction with ammonium metavanadate to form peroxovanadium cations.[72] All CA experiments were performed in duplicate.

The occurrence of the hydrogen evolution reaction (HER) was assessed using multi-chrono-amperometry (MCA) experiments in the same flow-through module used for $H_2O_2$ electrogeneration. In the MCA experiments, potentials of +0.5, 0.0, −0.5, −1, and −1.5 V vs. SHE were applied sequentially for 300 s each to the Ag-PAI membrane as the working electrode while monitoring the flowing current over time and measuring the cell potential using an additional multimeter connected between the working and counter electrode.

### 2.6. Membrane Performance Test Experiments

The performance of pristine PAI and Ag-PAI membranes was evaluated using a cross-flow filtration setup at a pressure of 20 psi and a feed flow rate of 2.4 L $min^{-1}$. The setup was equipped with a circulating water bath (ISO temp3013, Fisher Scientific) to control the feed temperature. To assess the dye rejection performance of the membrane under an electrical potential (ranging from 0 to 7 V), 20 ppm solutions of RR120 and RB were filtered. An electrical potential was applied between the stainless-steel electrode (anode) and the Ag-PAI membrane's (cathode) surface. The volumetric permeate flux and dye rejection were calculated by Equations (1) and (2), respectively.

$$J_W = \frac{\Delta m}{\rho A_m \Delta t} \tag{1}$$

where $\Delta m$ represents the mass difference, $\rho$ was the membrane permeate density, $A_{m\ \mathrm{was}}$ the membrane surface area (20.25 $cm^2$), and $\Delta t$ denotes the filtration time.

$$R\,(\%) = \left(1 - \frac{C_p}{C_f}\right) \times 100 \tag{2}$$

Here, $C_p$ and $C_f$ represent the dye concentration in the permeate and feed solutions, respectively, measured by UV–Vis spectrophotometry.

The antifouling tests were conducted based on a three-step procedure to evaluate membrane performance under an applied electric potential. Initially, DI water was filtered for 20 min to stabilize the permeate flux before introducing the foulant into the feed solution. Permeate was collected on a digital balance (ME4002, Mettler Toledo), with data recorded on a computer at 15-s intervals. Following this, the feed solution was replaced with a 200 ppm foulant solution, and the permeate flux of the foulant solution ($J_{wf}$) was measured over 6 h. After fouling, the membrane surface was washed with DI water for 20 min at the same flow rate and applied pressure (20 psi) as in the fouling step. No additional pressure was applied beyond this point. The same DC electrical potential used in the fouling step was applied to the membrane during the cleaning step. The pure water flux of the cleaned membrane ($J_{w2}$) was then measured after the washing step.

To evaluate the antifouling property of the membranes, the total flux decline ratio ($FDR_t$) and flux recovery ratio ($FRR$) were calculated according to Equations (3) and (4), respectively, as follows:

$$FDR_t = 1 - \frac{J_{wf}}{J_{w1}} \tag{3}$$

$$FRR = \frac{J_{w2}}{J_{w1}} \tag{4}$$

The release of silver ions from the electro-conductive membrane was assessed through both batch and dynamic filtration experiments. In the batch test, a membrane sample (1 $cm^2$) was

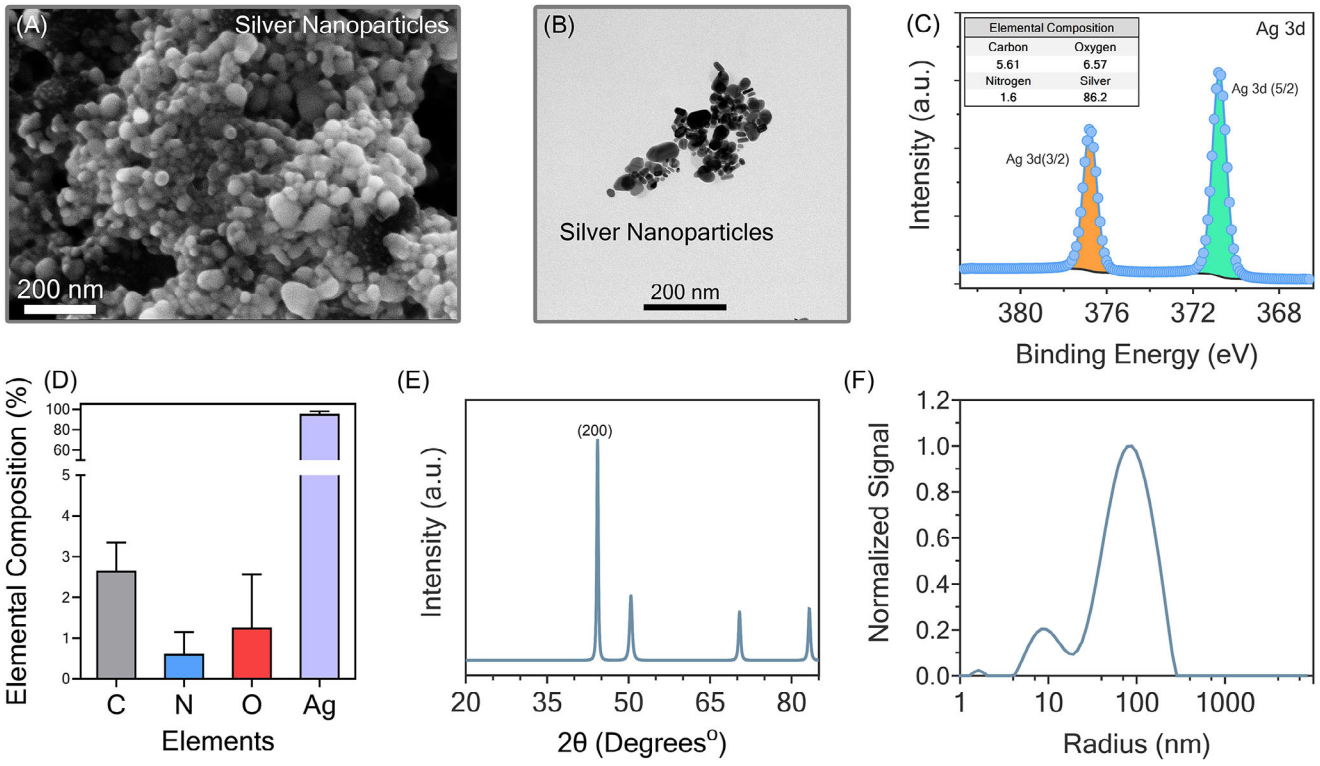


**Figure 3.** Characterization of Ag nanoparticles (Ag-NPS). A,B) SEM and TEM images showing Ag-NP morphology. C) High-resolution XPS Ag 3d spectrum with peaks at ≈368.2 eV (Ag $3d_{5/2}$) and ≈374.2 eV (Ag $3d_{3/2}$) (inset: elemental composition of Ag-NPS). D) EDX analysis shows Ag as the dominant element. E) XRD pattern with a primary peak at 44.4° (200 plane) F) DLS size distribution indicating the hydrodynamic size of Ag-NPS.

immersed in 20 mL of DI water and shaken at 100 rpm at room temperature. To monitor $Ag^+$ release, the DI water was replaced every 24 h, and the collected samples were analyzed using ICP analysis.

For the dynamic release test, a membrane with an active surface area of 20.25 $cm^2$ was subjected to filtration under the same conditions used in the performance test: an applied voltage of 3 V, flow of 2.4 L $min^{-1}$, and a pressure of 20 psi. The experiment was conducted continuously for 24 h, with permeate samples collected every 2 h to monitor silver release over time. All samples were analyzed using ICP techniques.

### 2.7. Antibacterial Assessment Methods of Membranes

The antibacterial properties of pristine PAI and Ag-PAI membranes were investigated via colony-forming unit (CFU) enumeration and disc inhibition zone against (*E. Coli* FAMP). The inhibition ratio *IR*(%) from the CFU enumeration test was calculated using Equation 5:

$$IR\,(\%) = \left(1 - \frac{N_{CFU(Ag-PAI)}}{N_{CFU(PAI)}}\right) \times 100 \qquad (5)$$

where $N_{CFU(Ag-PAI)}$ and $N_{CFU(Ag-PAI)}$ are the number of colonies formed on the agar plates for modified (Ag-PAI) and pristine (PAI) samples, respectively. See detailed procedure in Section S6 (Supporting Information).

## 3. Results and Discussions

### 3.1. Characterization of Silver Nanoparticles

SEM and TEM results (**Figure** 3A,B) show that the silver nanoparticles are mostly spherical and form a compact, interconnected network on the membrane surface. This connected structure likely results from interparticle contact rather than uncontrolled agglomeration. Such network formation was beneficial, as it facilitates the creation of continuous conductive pathways, thereby enhancing the membrane's overall electrical conductivity.[73] Furthermore, the size distribution of silver nanoparticles determined by DLS (Figure 3F) indicates a hydrodynamic radius ranging from 30 to 100 nm, with a mean particle size of 57.5 nm.

Additionally, the XPS analysis of the nanoparticles is shown in Figure 3C. The deconvolution of Ag 3d reveals two distinct peaks at 368.2 eV (Ag $3d_{5/2}$) and 374.2 eV (Ag $3d_{3/2}$), characteristic of silver.[47] The atomic concentration of Ag was 86.2%, indicating its dominance in the structure. Furthermore, the EDX analysis (Figure 3D) revealed a prominent peak ≈3 keV, corresponding to silver, associated with the surface plasmon resonance effect.[74] This signal indicates that the sample contains over 95 wt.% silver, which aligns with the XPS results. The XRD pattern of the silver nanoparticles (Figure 3E), recorded in the 2$\theta$ range of 20° to 90°, shows a distinct peak at 44.4°, corresponding to the (200) crystallographic plane of silver. This peak matches the JCPDS (Card No. 87–0597), confirming the face-centered cubic (FCC) structure of silver.[75]

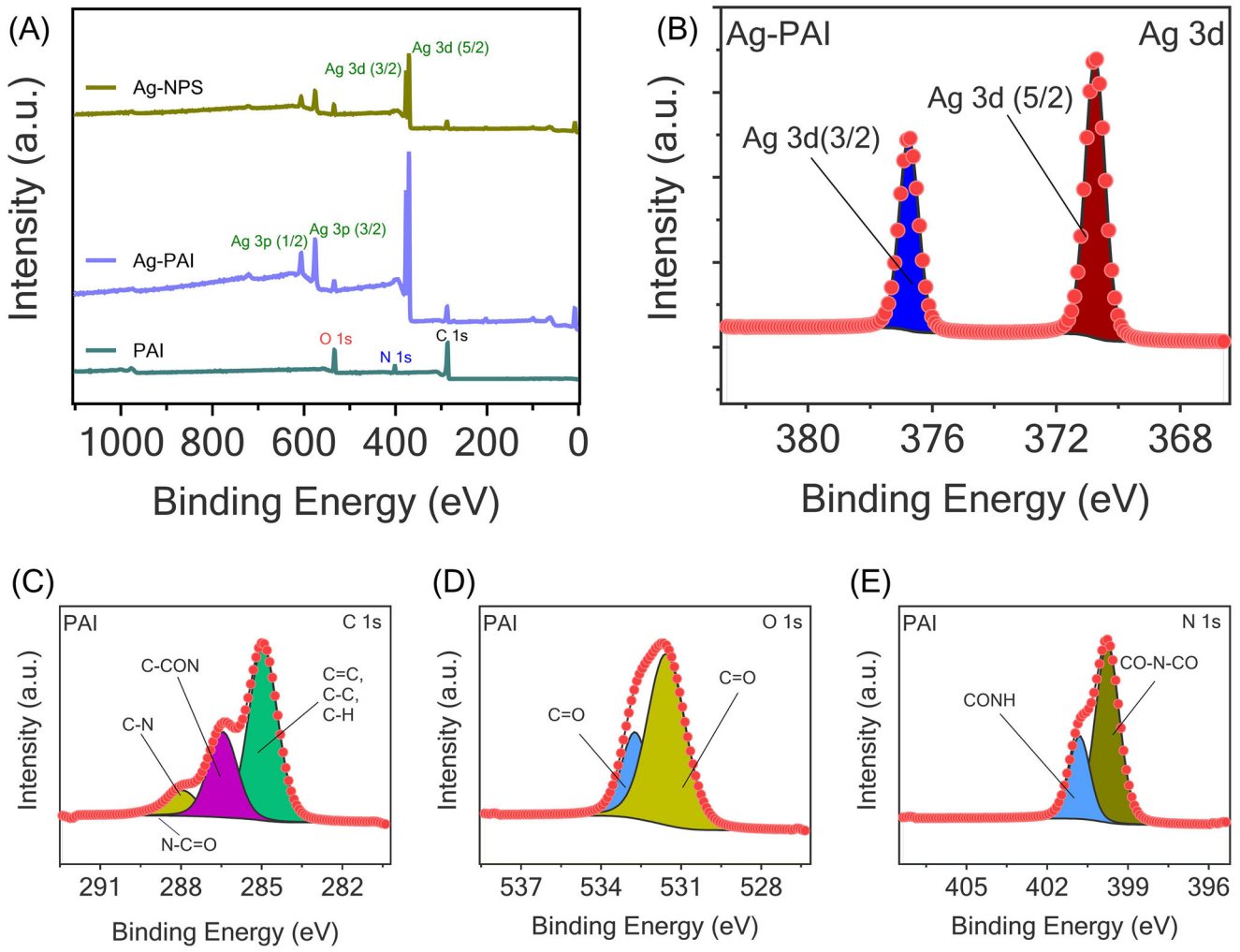


**Figure 4.** XPS analysis of pristine PAI, Ag-PAI, and Ag-NPs. A) Survey spectra showing Ag 3d and Ag 3p peaks after silver incorporation. B) High-resolution Ag 3d spectra C) C 1s spectrum of PAI with peaks for aromatic C═C/C–C/C–H, imide C–CON, C–N, and N–C═O. D) O 1s spectrum showing imide and amide C═O bonds. E) N 1s spectrum with imide (—CO—N—CO—) and amide (—CONH—) peaks.

### 3.2. Surface Characterization of the Fabricated Membranes

The XPS survey spectra of the prepared membranes in **Figure 4** reveal the existence of three primary elements: carbon, oxygen, and nitrogen, positioned ≈285, 531, and 400 eV, respectively.[76,77] **Table 1** presents the elemental compositions of the Ag NPS, pristine PAI, and Ag-coated PAI membranes, as determined from the XPS analysis. The high-resolution C 1s spectrum (Figure 4C) shows a ≈284.6 eV peak for C═C, C—C, and C—H bonds in the aromatic rings, contributing to polymer stability.[77] The ≈286 eV peak corresponds to C–CON from the imide (—CO—N—CO—) structure, reinforcing the backbone. The presence of C–N bonds (≈287.6 eV) represents amide (-CONH-) and imide (-CO-N-CO-) linkages, which can be attributed to the nitrogen-carbon connectivity within the polymer.[78] Finally, the peak at ≈288.7 eV, assigned to N—C═O, verifies the presence of imide and amide groups.[79,80] The high resolution O 1s spectrum (Figure 4D) shows C═O (≈531.5 eV) from imide (-CO-N-CO-) and C═O (≈532.7 eV) from amide (-CONH-), representing both linkages.[81,82] The high-resolution N 1s spectrum (Figure 4E) shows N-C (≈399.8 eV) from imide and amide, as well as N—H (≈400.8 eV) from amide, indicating the polymer's characteristic backbone.[81] These findings support the polyamide-imide structure.

**Table 1.** Comparative elemental compositions of the Ag NPS, pristine PAI, and Ag-coated PAI membranes as determined by XPS analysis.

| Membrane\Atom | Carbon | Oxygen | Nitrogen | Silver |
|---|---|---|---|---|
| Ag NPS | 5.61 | 6.57 | 1.6 | 86.2 |
| PAI | 56.97 | 34.34 | 8.7 | 0 |
| Ag-PAI | 4.84 | 3.53 | 3.63 | 88 |

The Ag-PAI membrane shows strong Ag 3d and Ag 3p peaks (Figure 4B).[83,84] Notably, the Ag-PAI spectrum resembles the Ag-NPS spectrum (Figure 4A). The Ag content in Ag-PAI (88%) is slightly higher than in Ag-NPS (86.2%), and also the C (4.84%

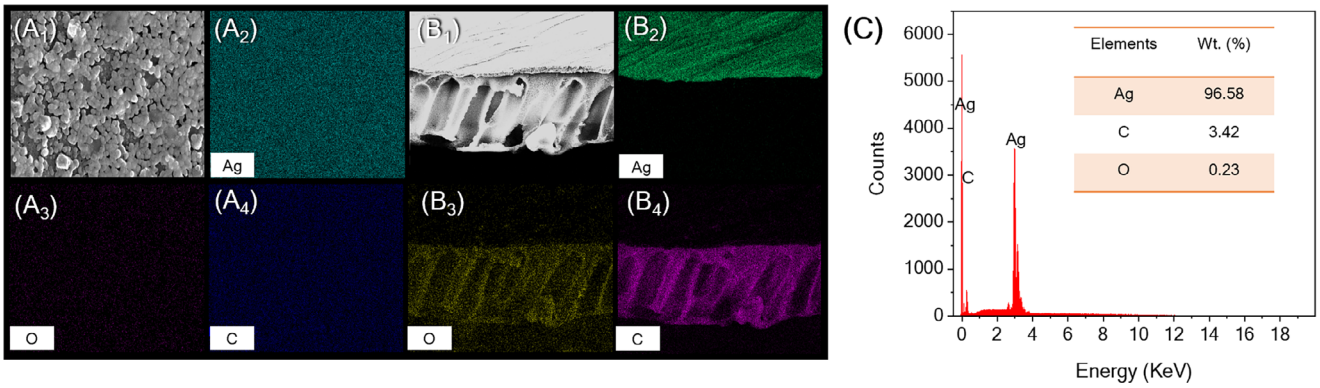


**Figure 5.** $A_1$–$A_4$) EDX mapping analysis for three elements: ($A_2$) silver, ($A_3$) oxygen, and ($A_4$) carbon from the corresponding top surface FE-SEM image; $B_1$-$B_4$) cross-sectional view of the Ag-PAI membrane coating layer with STEM-EDX mapping showing the same elements; C) elemental compositions of Ag-PAI membrane.

vs. 5.61%), O (3.53% vs. 6.57%), and N (3.63% vs. 1.6%) contents differ slightly (Table 1). This similar XPS spectra between Ag-NPS and Ag-PAI membrane suggests that the Ag-NPS coated the membrane surface entirely.

The EDX mapping confirmed the presence of Ag on the membrane's surface. As shown in **Figure 5C**, the average Ag loading, calculated from the EDX analysis, was found to be as high as 96% by weight on the Ag-coated membrane. Figure 5A1–A4 and Figure $5B_1$–$B_4$ provide explicit representations of the EDX scans obtained from the top and cross-sectional views of the silver-modified membrane, respectively. The images revealed that while the cross-section of the membrane contains higher levels of C and O elements, the top surface is predominantly composed of Ag.

As illustrated in **Figure 6A**, there was a 12-degree reduction in the WCA of the Ag-PAI membrane compared to the pristine PAI membrane, shifting from 55° to 43°. Coating membrane surfaces with hydrophilic nanomaterials such as AgNPs limits the adhesion of hydrophobic organic foulants.[85] This can be achieved through two primary mechanisms: modifying surface roughness and enhancing hydrophilicity.[86] Both properties facilitate water passage through the membrane and establish a hydration layer that prevents foulants from attaching to the membrane surface. As can be seen in Figure 6B, the surface roughness of the membranes increased upon Ag coating, from ≈20 nm in pristine PAI to ≈39 nm in Ag-PAI membranes. The increased roughness, caused by silver nanoparticles, enhanced hydrophilicity as predicted by the Wenzel equation.[87] According to this theory, in hydrophilic materials, when the WCA on a surface is below 90°, increased surface roughness leads to a decrease in WCA, thereby improving surface wettability. These observations align with the WCA measurements, confirming that increased surface roughness enhanced the membrane's hydrophilicity.[88]

Figure 6C displays the zeta potential of pristine PAI and Ag-PAI membranes, conducted using a zeta potential analyzer. The data revealed that both membranes exhibited a negative charge across the pH range of 4.0 to 9.0. Furthermore, the magnitude of this negative charge increased with rising pH values. The pristine PAI membrane showed minor fluctuations (6 mV), while the Ag-PAI membrane exhibited an isoelectric point at pH = 4.5 and a less negative potential of −15 mV at pH = 9.0. Coating the PAI membrane with silver alters its charge characteristics, as the positive charge of silver nanoparticles reduces the overall negative potential. In the case of the Ag-PAI membrane, although it exhibits a less negative surface charge compared to pristine PAI, the electrochemical reactions occurring under applied voltage, such as HER, [89] play a critical role in enhancing antifouling performance [82]. Also, under cathodic conditions, water electrolysis generates hydroxide ions ($OH^-$), leading to a locally increased pH near the Ag-PAI membrane surface. This elevated pH can influence the surface charge by increasing the negative potential in the membrane.[90] Additionally, the presence of silver demonstrates good stability under alkaline conditions (**Figure 8A**), which not only preserves the membrane structure but also facilitates electron transfer. Together, these effects enhance electrochemical activity and antifouling performance. The electron density test directly measures the functional groups contributing to the membrane's chemical reactivity at different pH levels (Figure 6D). At pH 7, the pristine PAI membrane exhibited a higher electron density (≈52.9 sites $nm^{-2}$) than the Ag-PAI membrane (≈33.2 sites $nm^{-2}$). This higher density in the pristine PAI membrane is attributed to secondary amide groups (−HNC═O), which are less prone to losing hydrogen at pH 7. In contrast, the silver nanoparticles (Ag NPs) coating the Ag-PAI membrane reduce the overall density by neutralizing secondary amide groups through direct bonding with the silver nanoparticles. At pH 10.5, the pristine PAI membrane reached a charge density of ≈42 sites $nm^{-2}$, while the Ag-PAI membrane had ≈24.2 sites $nm^{-2}$. The minor decrease observed in the Ag-PAI membrane indicates that the silver coating limits the ionization potential and forms ionic bonds with the secondary amide groups that help with their strong bond with the PAI layer. Amide groups contain two potential coordination sites for metal ions, such as $Ag^+$: the carbonyl oxygen and the amino nitrogen. Among these, the carbonyl oxygen is generally the preferred coordination site due to its higher electron density and accessibility, often resulting in weakening of the C═O bond and relative strengthening of the C—N bond upon coordination.[91] Depending on the molecular environment, silver ions can coordinate in either a monodentate mode (binding to either O or N) or a bidentate mode (simultaneous coordination to both O and N within the amide group). In our study, the PAI support matrix contains secondary amide groups, which are known to stabilize

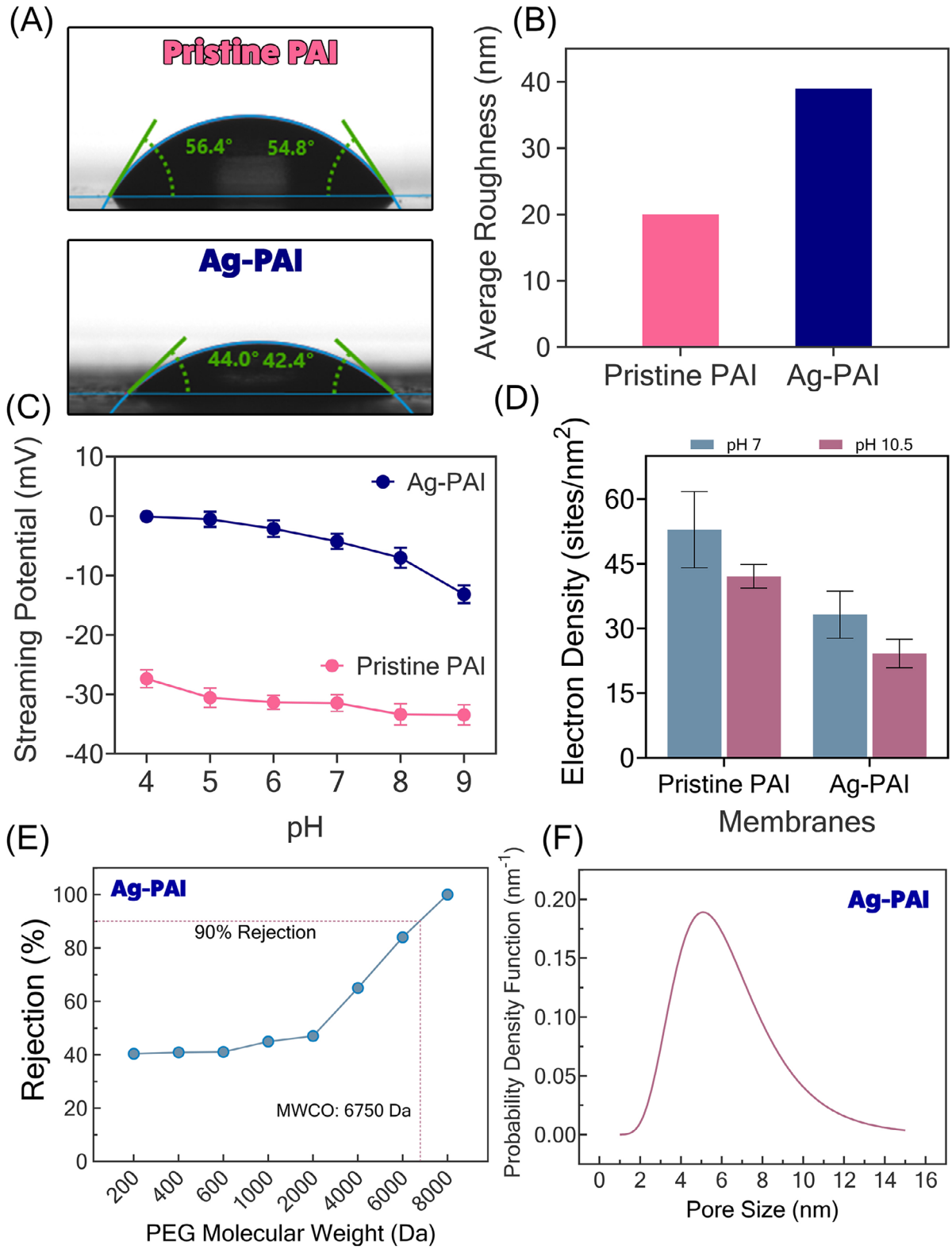


**Figure 6.** A) WCA measurements of the pristine PAI membrane (top) and Ag-PAI membrane (bottom); and B) AFM results show increased average and RMS roughness in Ag-PAI membranes compared to pristine PAI, highlighting the impact of silver nanoparticle coating on surface morphology. C) The zeta potential of membranes as a function of solution pH. D) The charge density in the structure of pristine and modified membranes. (charge density (Sites $nm^{-2}$). E) The MWCO and F) Pore size distribution of Ag-PAI membrane.

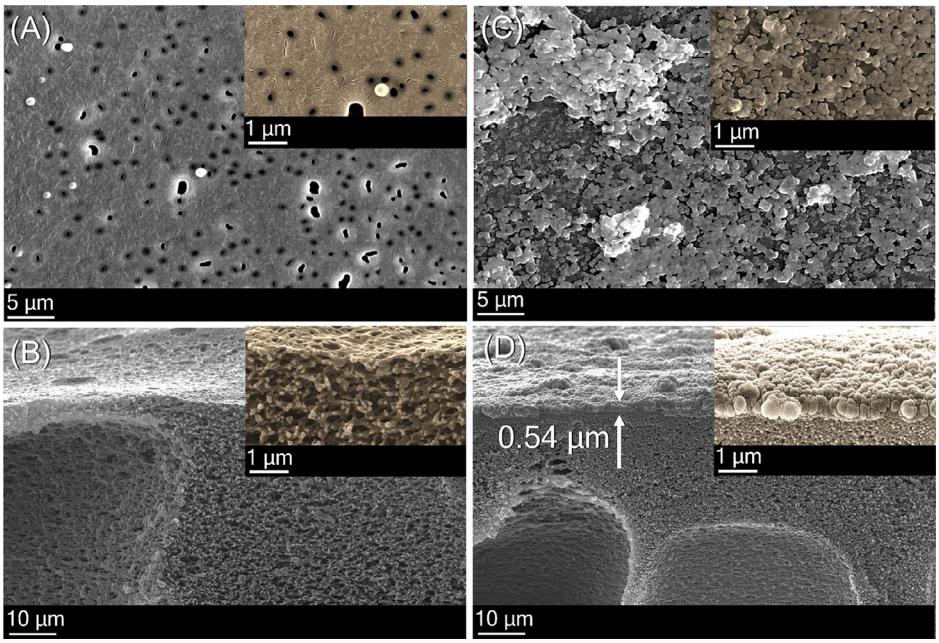


**Figure 7.** A) Top-surface and B) cross-sectional FE-SEM images of the prepared PAI support layer; C) top-surface and D) cross-sectional FE-SEM images of the Ag-PAI membrane, demonstrating a silver coating thickness of ≈0.54 µm.

coordination complexes with $Ag^+$. This interaction has been previously reported in coordination chemistry and metal–polymer interface studies.[92,93]

The MWCO and pore size distribution of the Ag-PAI membrane were evaluated by filtering PEG solutions with molecular weights ranging from 200 to 8000 Da. The molecular weight corresponding to 90% rejection is defined as the MWCO, which was determined to be 6750 Da (Figure 6E). Additionally, the probability density function plotted against pore size (Figure 6F) demonstrates that the membrane has an effective mean pore size of 5 nm and exhibits a moderately narrow pore size distribution. This analysis provides further insight into the membrane's separation performance for neutral solutes, where electrostatic interactions are negligible and size exclusion dominates. The membrane's ability to retain PEG molecules above 6750 Da indicates that similarly sized neutral compounds would be effectively rejected, while smaller molecules are more likely to permeate through the membrane.

FE-SEM analyzed the surface morphology of the membranes before and after Ag-coating (**Figure 7**). The main objective of this study is to use the electro-conductivity and antibacterial properties of Ag-NPS for the membrane's functionality. Therefore, it is essential that Ag-NPS cover the entire membrane surface and form a strong bond with the PAI layer. In both the top surface and cross-section FE-SEM analysis, a distinct Ag-coating layer on the PAI support can be seen (with a measured thickness of 0.54 µm).

### 3.3. Electrochemical Properties and Filtration Performance of the Membranes

Due to the non-conductive nature of the PAI polymer, the pristine PAI membrane exhibited a low electrical conductivity of $2.215 \times 10^{-5}$ S cm$^{-1}$. In contrast, the Ag-PAI membrane showed a significant increase in conductivity, exceeding $5.6 \times 10^4$ S cm$^{-1}$. This substantial enhancement can be attributed to the metallic nature of silver nanoparticles, which form conductive pathways for rapid charge transfer across the membrane. However, acidic conditions may also influence membrane conductivity.

As depicted in **Figure 8A**, the electrical conductivity of the Ag-PAI membrane remained stable at $\approx 5.6 \times 10^4$ S cm$^{-1}$ in different acidic (pH = 2), neutral (pH = 7), and alkaline (pH = 10) conditions. The Ag-PAI membrane exhibited cathodic stability but demonstrated anodic instability when subjected to positive electric potential. This anodic instability resulted from the rapid oxidation of Ag nanoparticles, which caused the Ag coating to peel off and reduced the membrane's electrical conductivity. Notably, a similar phenomenon has been reported for CNT coatings, which also exhibit instability during anodic operation modes due to CNT oxidation.[94]

LSV and EIS tests were conducted to examine the electrochemical behavior of the Ag-modified membrane. Figure 8B represents the Nyquist plot, which provides information about the electrochemical resistive and capacitive behavior of the electrochemical cell. In the high-frequency region, the *x*-axis intercept corresponds to a resistance of ≈5 Ω. This resistance is primarily attributed to the electrolyte (50 mM of $Na_2SO_4$) and all the configurations, the electrode distance and area. The ohmic resistance also reflects the intrinsic and contact resistance of the electrode material. Since the counter electrode (Pt-coated expanded metal) has high electrical conductivity, it can be inferred that the Ag-PAI membrane used as the working electrode also exhibits high electrical conductivity.

Figure 8C shows the LSV data for the Ag-PAI membrane under $O_2$ and $N_2$-saturated medium. A greater current decrease was observed at 0.5 V vs. SHE under $O_2$ saturation compared to $N_2$,

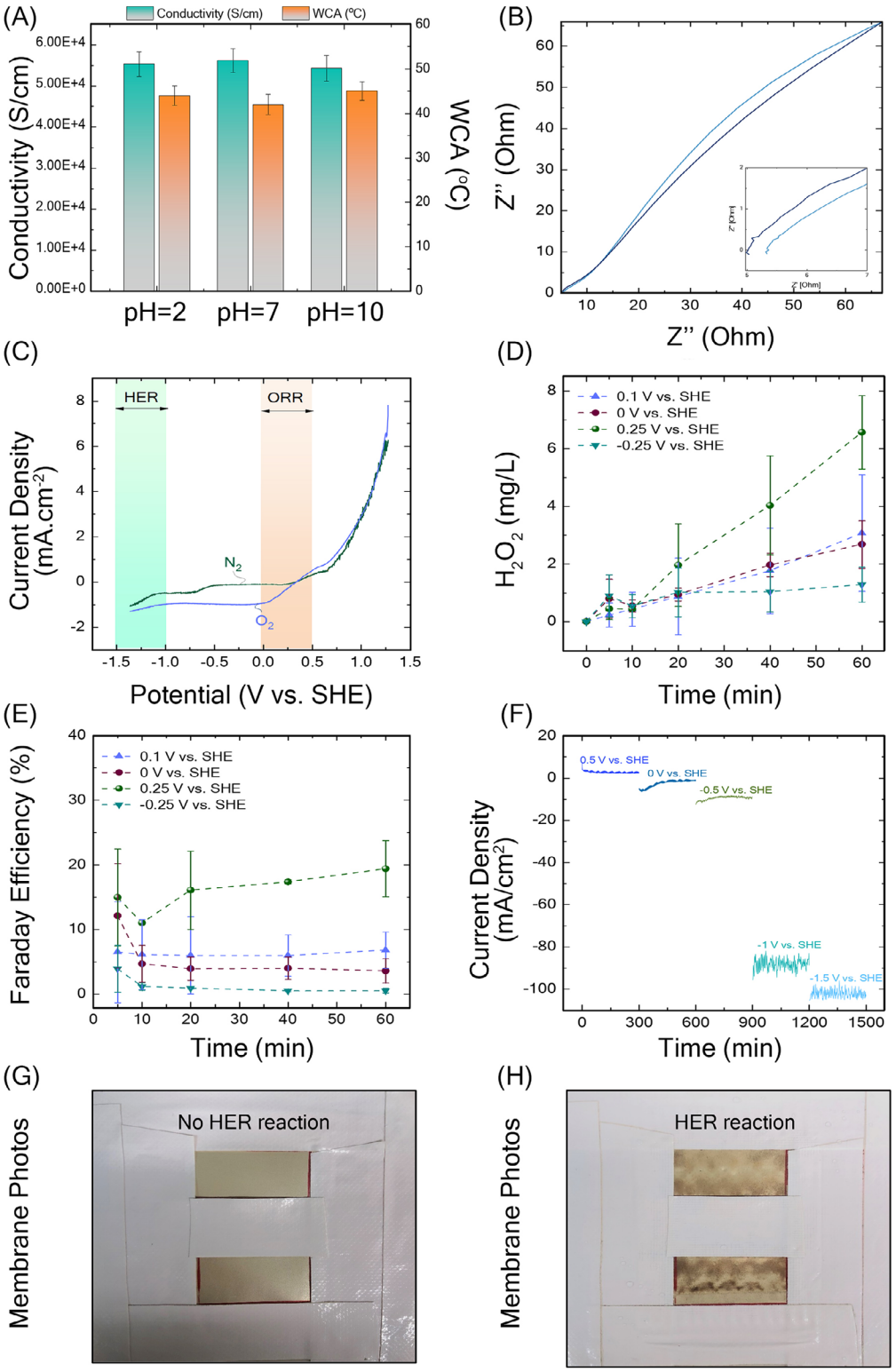


**Figure 8.** A) WCA measurement and electrical conductivity measurements after a stability test (48 h immersion in solutions with various pH; B) the EIS and C) the LSV analyses conducted in the flow-through module using the Ag-coated PAI membrane as the working electrode, with 50 mM $Na_2SO_4$ served as an electrolyte circulated at a 50 mL $min^{-1}$ flow rate; D) the concentration of $H_2O_2$ and E) corresponding Faraday efficiency measured over CA experiments in a flow-through module divided by a cation exchange membrane. 50 and 500 mM of $Na_2SO_4$ and $H_2SO_4$ were circulated at 50 mL $min^{-1}$ as catholyte and anolyte, respectively; F) monitored current density at different applied cathodic potentials during MCA analysis using the divided flow-through module. The strong fluctuations in monitored current density observed at more negative cathodic potentials were caused by bubble formation on the electrode surface; G) photographs of Ag-PAI membranes before and H) after MCA experiments.

indicating the occurrence of oxygen reduction reaction (ORR) on the Ag-PAI membrane surface. After reaching the plateau, the current showed another decline at cathodic potentials lower than −1.0 V vs. SHE under both $O_2$ and $N_2$ saturation, which can be attributed to the onset potential for HER. The LSV results indicate that ORR occurs within the potential window of +0.5 to 0.0 V vs. SHE.

Figure 8D displays the concentration of $H_2O_2$ formed in the flow-through module at a constant potential of +0.25, +0.1, 0.0, and −0.25 V vs. SHE over 1-h experiments. Considering the average values, the highest average $H_2O_2$ concentration of 6.6 ± 1.3 ppm was achieved at an applied cathodic potential of 0.25 V vs. SHE. In comparison, the decrease in potential to −0.25 V resulted in the lowest $H_2O_2$ concentration of 1.3 ± 0.6 ppm by the end of the experiments. Based on Figure 8E, the Faraday efficiency for $H_2O_2$ electro-generation reached its maximum of 20 ± 4.3 % at 0.25 V vs. SHE and declined with decreasing the cathodic potential. Although these results show the potential for $H_2O_2$ formation on the Ag-PAI membrane electrodes, the $H_2O_2$ concentration was relatively low and significantly decreased as the applied cathodic potential dropped.

Figure 8F represents the MCA data for the Ag-PAI electrodes at cathodic potentials of 0.5, 0.0, −0.5, −1.0, and −1.5 V vs. SHE. The monitored current density stayed below 20 mA $cm^{-2}$ for applied potentials from 0.5 to −0.5 V but increased drastically to 90 mA $cm^{-2}$ at −1.0 V vs. SHE. This sharp increase in current density is attributed to the HER on the Ag-PAI membrane. Fluctuating current signals, typical of bubble formation, became more pronounced at −1.5 V vs. SHE. Visible bubble formation occurred in the catholyte solution at potentials of −0.5, −1.0, and −1.5 V vs. SHE. The measured cell potentials for the MCA experiments were 0.62, 1.64, 2.24, 3.4, and 4.2 V for applied cathodic potentials of 0.5, 0.0, −0.5, −1.0, and −1.5 V vs. SHE, respectively.

Hence, increasing the cell potential promotes the formation of $H_2$ bubbles, which can facilitate the detachment of foulants from the membrane surface during a membrane filtration process. The primary antifouling mechanisms during filtration include electrostatic repulsion between negatively charged foulants and the membrane surface, as well as $H_2$ bubble formation at elevated cell potentials. Photographs of the fresh Ag-PAI membranes before and after the MCA experiment are presented in Figure 8G,H, respectively. Compared to the sophisticated methods required for preparing electrocatalysts to improve antifouling performance, the HER facilitated by silver nanoparticles offers a facile, easily scalable deposition approach.[95,96]

### 3.4. Dye Separation and Antifouling Performance of Membranes Under Electric Potential, and Evaluation of Membrane Stability

The filtration performance of the PAI and electro-conductive Ag-PAI membranes was evaluated using a two-electrode cross-flow filtration setup, focusing on dye rejection as a key parameter in assessing membrane performance under applied electric potentials. In this setup, the Ag-PAI membrane served as the cathode, while stainless steel was used as the anode. To assess the influence of electrical assistance on the modified membrane, two negatively charged dyes, RB (MW: 991.82 Da) and RR120 (MW: 1774.15 Da), were filtered at incremental potentials ranging from 0 to 7 V.

**Figure 9A,B** shows the filtration performance of the Ag-coated membrane against RR120 and RB as a function of applied voltage. Dye rejection increased with applied potential, by 14% for RR120 and 32% for RB, though the trend was nonlinear, as higher voltages did not yield proportionally greater improvements. This behavior can be attributed to bubble dynamics, where increased gas evolution at higher voltages produces larger hydrogen bubbles that may disrupt the uniform electric field distribution, limiting further rejection improvement.[97] In addition to the bubble effect, the greater rejection improvement observed for RB compared to RR120 is likely due to its smaller molecular size and higher electrophoretic mobility, making it more responsive to the applied electric field.[98] Permeation flux remained stable, increasing slightly from ≈90 LMH to 100 LMH. This slight flux increase may also result from localized heating at the membrane surface under applied voltage, which reduces solution viscosity and facilitates water permeation.[99]

These results suggest that applying an external electric field enhanced rejection performance while maintaining membrane permeability. This can be explained by the findings from MCA experiments, which suggest that the membrane surface acquires a more negative charge when an electric potential is applied between the modified membrane (cathode) and the anode. The increased current density and electron transfer in the Ag-PAI membrane enhance the local negative surface charge, which intensifies electrostatic repulsion between the membrane and negatively charged dyes, leading to improved dye rejection.[100]

Although only anionic dyes were evaluated in this study, the membrane's near-neutral surface charge at pH 7 implies that electrostatic repulsion toward cationic dyes would be limited. In such cases, dye rejection would primarily depend on steric hindrance and molecular size. This behavior has been noted in other studies, where size exclusion dominated dye retention even when membrane-solute charge interactions were not favorable, indicating that molecular dimensions can outweigh charge effects when electrostatic forces are weak.[101,102]

The normalized fluxes versus time are shown in Figure 9C. The water flux of the pristine PAI membrane (0 V) declined more rapidly than that of the Ag-PAI membrane under applied voltage. The organic fouling test demonstrated that the pristine PAI membrane lost ≈60% of its initial flux, while the modified membrane experienced a lower flux decline, reaching a minimum of 43% at 7 V. The antifouling performance of the pristine PAI and Ag-PAI membranes was evaluated by monitoring flux decline ratio (FDR) during a 6-h filtration of SA/$CaCl_2$ solution using the same cross-flow setup (Figure 9D). Afterward, the feed solution was replaced with DI water, and the membrane underwent a 20-min cleaning process. Following this cleaning step, the corresponding FRR was assessed by determining the recovered water flux after washing using Equation (4). Like the filtration experiment, the membrane was exposed to an external voltage ranging from 0 to 7 V with increments of 2 V. Simultaneously, the FRR (Figure 9D) values increased with the rising electrical potential in the modified Ag-PAI membrane. Compared to the pristine PAI (without voltage) membrane with an FRR of ≈49%, the Ag-PAI under electrical voltage exhibited an increased FRR, ranging from 43% to 80%. It should be emphasized that these

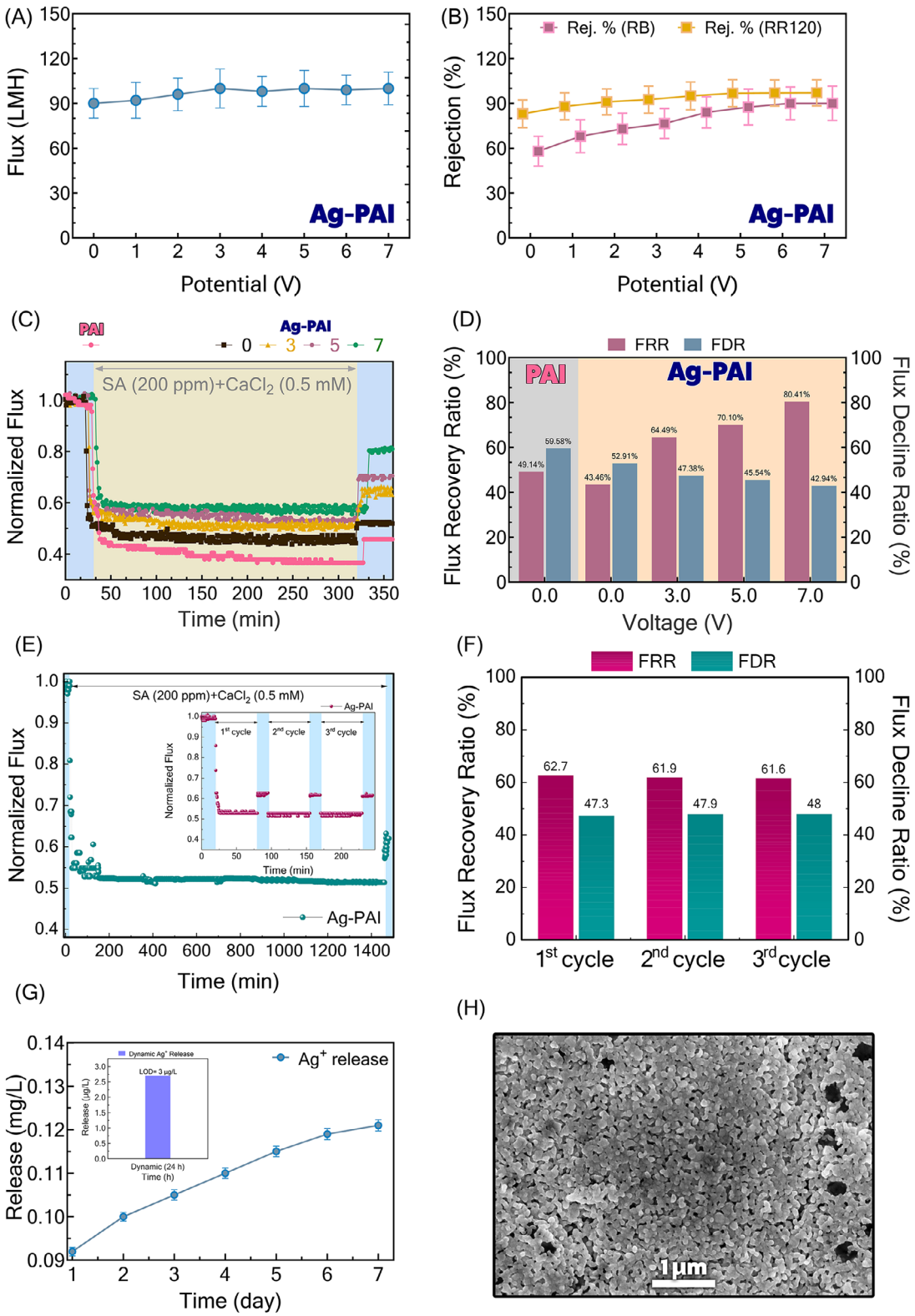


**Figure 9.** A) Water flux and B) dye rejection performance of the Ag-PAI membrane with electrochemical assistance, using RR120 and RB as dye solutions; C) antifouling behavior of the pristine PAI membrane ($M_0$) and Ag-PAI membranes over 6 h of continuous filtration of 200 ppm SA/$CaCl_2$ at varying voltage levels; and D) FDR and FRR of the membranes under different voltages, showing the effectiveness of higher voltages in enhancing antifouling properties; E) long-term and cyclic anifouling performance of the Ag-PAI membrane under an applied potential of 3 V; F) FDR and FRR of the Ag-PAI membrane during cyclic testing under 3 V; G) long-term silver release profile of the Ag-PAI membrane under batch and dynamic filtration. Subpanel: 24 h dynamic release (3 V, 20 psi); H) FE-SEM image of the membrane after seven days of silver release.

antifouling results are specific to organic fouling, represented by sodium alginate and calcium chloride as model foulants. The membrane's effectiveness against other fouling types, such as inorganic or colloidal foulants, requires further investigation. These results support the enhanced antifouling properties of the electro-conductive membrane under the tested conditions.

The improved antifouling properties of the Ag-PAI membrane with increasing voltage can be attributed to several factors: (1) the negative surface charge of the Ag-PAI membrane generates electrostatic repulsion, which inhibits negatively charged foulants from adhering to the membrane surface; (2) the production of hydrogen ($H_2$) bubbles on the electro-conductive membrane surface effectively removes the cake layer; and (3) enhanced hydrophilicity leads to the formation of a hydration barrier that prevents the attachment of foulants.[103,19]

Although increased surface roughness due to silver nanoparticle deposition could theoretically promote bubble attachment, in this case, the enhanced hydrophilicity and hydration layer counteract this effect. Furthermore, the transient nature of bubble formation during HER and the increased gas generation rate at higher applied voltages, as demonstrated by the MCA experiments, further prevent stable foulant accumulation on the membrane surface.[104,105] Therefore, the proposed electrically enhanced approach for reducing fouling propensity is a straightforward strategy that eliminates the need for chemicals and consumes less energy.

Cyclic and long-term fouling tests were performed at 3 V to further assess the Ag-PAI membrane's resistance to organic fouling. The cyclic test consisted of three consecutive steps (1 h fouling followed by a 20-min wash). As shown in Figure 9E,F, the FDR slightly increased from 47.3% to 48% over the three cycles, while the FRR showed only a minor decline from 62.7% in the first cycle to 61.9% and 61.6% in the second and third cycles, respectively. In the long-term fouling test (24 h), the membrane maintained stable performance with an FDR of 48.6% and an FRR of 62%, demonstrating the membrane's durability under prolonged and repeated fouling conditions. These findings suggest that the application of an electric field effectively repels foulants from the surface of the electro-conductive membrane, helping to maintain its filtration performance over time. Moreover, the fouling behavior of the membrane under an applied electric field remained controllable, indicating reliable antifouling functionality during extended operation. Importantly, although only a single AgNP size (average 57.5 nm) was utilized in this study, previous research has shown that silver nanoparticles within the 30–70 nm range consistently enhance antifouling performance by increasing membrane hydrophilicity and repelling organic foulants such as sodium alginate.[106,107,57] These effects are not very sensitive to small variations in particle size, particularly for non-biological fouling rather than microbial foulants.[108–111] Therefore, the enhanced antifouling behavior observed in this work likely results from the combined effects of the applied electric field and the optimized incorporation of AgNPs.

The long-term stability of silver on the coated membrane is essential for practical membrane applications. Monitoring $Ag^+$ ion release profile offers a measure of coating stability and membrane lifespan. As shown in Figure 9G, the initial silver release on the first day was ≈0.092 mg $L^{-1}$, corresponding to 0.0575% of the total 3.2 mg silver content on a 1 $cm^2$ membrane. Over the course of seven days, this value increased slightly to 1.2 mg $L^{-1}$, equivalent to only 0.075% of the total silver loading. This minimal release supports the membrane's stability, further confirmed by SEM analysis (Figure 9H), which reveals only a slight detachment of silver nanoparticles from the surface. Since the batch test was conducted over seven days using the same membrane, direct daily monitoring of the surface morphology was not feasible. Therefore, the final SEM image of the membrane, taken after seven days, is presented here, which is consistent with the findings reported in previous papers.[112,113]

"To provide a more accurate comparison, a dynamic silver release test was performed under the same conditions as the filtration process (3 V, 20 psi, 2.4 L $min^{-1}$) for 24 h. As shown in the subpanel of Figure 9G, the silver concentration in the permeate was below the detection limit (LOD 0.003 mg $L^{-1}$), confirming minimal release under operational conditions. In contrast, the static batch test, which is often used as a worst-case method, showed comparatively higher silver release. These results align with previous studies suggesting that batch methods tend to exaggerate silver leaching, whereas dynamic methods may underestimate it due to system adsorption and dilution effects".[114,115]

### 3.5. Antibacterial Assessment of Pristine and Modified Membranes

The intrinsic antibacterial properties of pristine and modified membranes were assessed via disc inhibition zone and CFU enumeration tests under static and suspension conditions, respectively. These tests were designed to evaluate the baseline antibacterial potential of the membranes rather than fully replicate dynamic filtration conditions. The attachment to bacterial cell membranes, intracellular damage caused by Ag NPs or released $Ag^+$ ions, and oxidative stress induction by generating reactive oxygen species (ROS) are the predominant antibacterial pathways of silver NPs.[116] The disc inhibition zone test revealed no visible inhibition region around the membrane coupons (**Figure 10A**), indicating that antibacterial agents remained immobilized under static conditions. This is likely due to the strong integration of silver nanoparticles within the polymer matrix, restricting the release of Ag NPs or $Ag^+$ ions for direct bacterial contact. The CFU enumeration test, performed under suspension mode, demonstrated a 57% inhibition rate after 1 h of bacterial exposure (Figure 10B). The observed inhibition rate could be due to the increased release rate of antibacterial agents under suspension mode compared to static mode, as seen in the disc inhibition zone results. Additionally, the more positively charged surface of the Ag-PAI membrane (compared to the pristine PAI membrane) enhanced the electrostatic attraction between the membrane surface and partially negatively charged bacterial cells. Therefore, a larger population of bacterial cells adhered to the surface of the Ag-PAI membrane, allowing the incorporated nanoparticles to cause cell damage either by directly harming the cells through released Ag NPs and $Ag^+$ ions or by disrupting metabolic cycles through surface oxidative stress.[117,118] It should be noted that the release rate of $Ag^+$ from the Ag-PAI membrane must be limited and controlled to sustain antibacterial activity while ensuring sufficient stability to maintain long-term functionality.

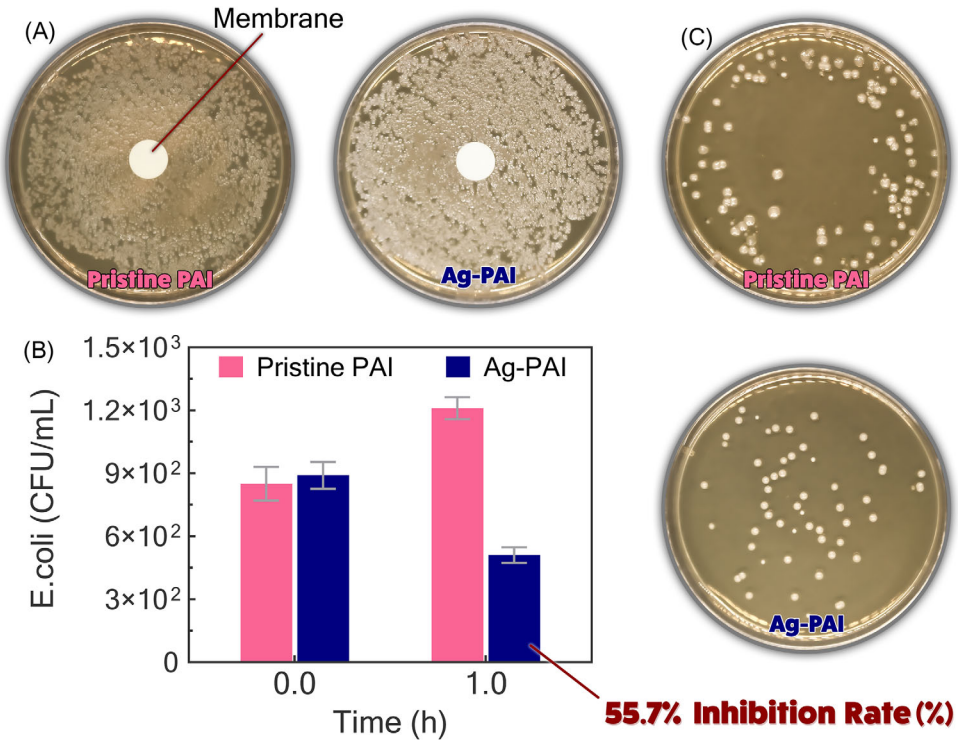


**Figure 10.** A) The inhibition zone test was conducted on both PAI and Ag-PAI membrane coupons, and B,C) the CFU enumeration results were obtained by exposing bacterial suspension (i.e., *E. coli*) to membrane coupons.

### 3.6. Comparison with Literature

**Table 2** presents a comparative analysis of our Ag-PAI membrane and previously reported electro-conductive membranes, highlighting the comprehensive scope of our evaluation. This includes electrochemical performance, dye rejection, antifouling behavior, electrical conductivity, water flux, and antibacterial activity, which are often addressed independently in earlier studies.

While certain recently reported electro-conductive membranes demonstrate higher rejection enhancements under specific conditions, the dye rejection improvement achieved by our membrane remains competitive, particularly at low applied voltages (2–3 V), where many studies report only modest increases of 4–11%. In contrast, our Ag-PAI membrane achieved up to a 14% increase in rejection within this low voltage range. For example, Ni-plated PVDF membranes required 7 V to achieve nearly a 20% improvement in dye rejection, whereas our Ag-PAI membrane achieved similar performance at just 5 V, underscoring its greater energy efficiency.

In terms of antifouling performance, our membrane exhibited a 21.5% increase in FRR at 3 V over 6 h, outperforming Memb-PAMPSA-EG/DBSA (10%) and PANI-rGO (16%). Additionally, it achieved a 5–6% reduction in FDR at the same voltage, a performance that compares favorably with MWCNTs-50, which showed less than 2% improvement and did not report FRR. Unlike studies that offer only qualitative or partial assessments, such as those on Ni-plated PVDF, our work provides quantitative validation of both FRR and FDR, positioning the Ag-PAI membrane among the most well-characterized electro-conductive membranes for antifouling performance. The membrane's high conductivity of $5.6 \times 10^4$ S cm$^{-1}$, which is substantially higher than MWCNTs-50 (0.00128 S cm$^{-1}$) and PANI-rGO (0.8453 S cm$^{-1}$), further enhances its electrochemical effectiveness. Moreover, it maintains a stable water flux of 100 LMH under applied voltage, unlike membranes that show only temporary flux improvements. The Ag-PAI membrane also achieved 55.7% *E. coli* inhibition, a level of antibacterial activity rarely observed in similar electro-conductive membrane studies.

Taken together, these results underscore the multifunctional capabilities of our Ag-PAI membrane. The combination of enhanced rejection, effective antifouling, superior conductivity, stable flux, and antibacterial properties establishes this membrane as a high-performing and energy-efficient alternative to existing electro-conductive membranes for water treatment applications.

### 3.7. Cost Analysis for the Fabrication of Ag-PAI Membranes

To assess scalability and cost-effectiveness, we compared silver-based membranes with alternatives such as carbon-based coatings (CNTs, graphene) and conductive polymers (PANI, MXene). Carbon-based materials offer a cost advantage ($5 to $600 CAD m$^{-2}$), but generally exhibit lower conductivity than silver and often require higher loadings or chemical functionalization to achieve comparable performance. They also present dispersion challenges in solvent systems, which may affect coating uniformity during spray deposition.[128] Conductive polymers such as PANI and emerging materials like MXene are similarly expensive or even more costly than silver, with costs ranging between $210 and $660 CAD m$^{-2}$, and are prone to chemical degradation

**Table 2.** Comparison of the performance of various electro-conductive membranes with the Ag-PAI membrane developed in this study.

| Membrane | Rejection Enhancement (%) | Antifouling Enhancement (%) | Electrical Conductivity [S $cm^{-1}$] | Water Flux (LMH) | Antibacterial Properties | Refs. |
|---|---|---|---|---|---|---|
| Ag-PAI | RR: (+7) at 2V, (+14) at 7 V<br>RB: (+14) at 2V, (+32) at 7 V | FDR: (+5–6) at 3 V, (+10) at 7 V<br>FRR (+21.5) at 3 V, (+37) at 7 V | $5.6 \times 10^4$ | 100 (stable) | 55.7% *E. coli* growth inhibition | This work |
| MWCNTs-50 | No enhanced yeast rejection. | FDR: (+2) at 2 V,<br>FRR: N/A | 0.00128 | Temporarily Increased from 90 to 220 | N/A | [119] |
| Ni-plating PVDF | Congo red: (+19-20) at 7 V | Lacked quantitative discussion | N/A | 202 | Lack of discussion | [120] |
| Memb-PAMPSA-EG/DBSA | N/A | FDR: (+16)<br>FRR: (+10)<br>Voltage: N/A | 0.001 | 357 | N/A | [22] |
| TDC10 | Orange G: (+4) at 3 V<br>Methyl Orange: (+17) at 3 V | N/A | 60 | 23 | N/A | [121] |
| PANI-MWNT | N/A | FDR: (+15) at 2 V<br>FRR:(+ 11.8) at 2 V | 7.32 | 596.6 | N/A | [122] |
| MF membrane | N/A | FDR: (+7) at 2 V<br>FRR: N/A | – | 1980 | N/A | [123] |
| PANI-rGO | TOC:<br>(+11-12) at 3 V | FDR: (+12) at 3 V<br>FRR: (+16) at 3 V | 0.8453 | 107.7 | N/A | [18] |
| RGO-MXene | Orange G: (+35.4) at 2 V | N/A | $110 \times 10^3$ | 62.1 | N/A | [124] |
| CNT-ECM | N/A | N/A | 34.9 | 14.7 | Complete bacterial inactivation at 2.5 V | [125] |
| Zeolite/CNS | Crystal violet: (+40) from 2 V to 3 V | N/A | 20 | 210 | N/A | [126] |
| PANI-DBSA | N/A | FDR: (+38) at 1 V<br>FRR: N/A | $2.2 \times 10^{-4}$ | 15.5 | N/A | [127] |

or oxidation, particularly under aqueous conditions.[129] In contrast, Ag-PAI membranes offer a balanced combination of high conductivity, excellent stability in water, and easy processability via spray coating.[130] While silver requires proper waste management protocols due to its environmental impact, the overall material cost remains competitive at \$75 CAD $m^{-2}$. The fabrication cost is consistent across all membrane types, estimated at \$33–37 CAD $m^{-2}$, which includes spray coating and solvents (e.g., DMAc, isopropanol at \$5–8 CAD $m^{-2}$). Additionally, the PAI support layer contributes significantly to the total material costs, accounting for ≈70–80% of the total material mass (\$0.75–1.75 CAD $g^{-1}$). The cost estimates presented in this section were derived from current market prices of key raw materials obtained from commercial suppliers.[131–135] Material consumption rates were calculated based on our experimental membrane fabrication process, where ≈30 grams of silver nanoparticles per square meter of membrane were required to achieve the desired conductive layer, along with corresponding amounts of PAI polymer and solvents. Solvent costs were estimated based on typical laboratory-scale casting practices, with high-purity DMAc and isopropanol contributing ≈\$5–8 CAD $m^{-2}$.[136,137] This combined approach provides a realistic, laboratory-scale estimation of both material and fabrication costs, which may vary with process optimization or large-scale production. Taken together, the total cost of Ag-PAI membranes is ≈\$108.75–\$112.75 CAD $m^{-2}$, which is competitive for specialized highly electro-conductive membranes. The cost analysis results are summarized in **Table 3**.

## 4. Conclusion

The electro-conductive Ag-PAI membranes were fabricated using a simple and scalable spray-coating technique. The application of silver coating noticeably enhanced the membrane's

**Table 3.** Cost analysis of Ag-PAI membranes and comparison with conventional carbon and polymer-coated membranes at the laboratory scale.

| Parameter | Ag-PAI Membranes | Carbon-coated Membranes | Polymer-coated membranes |
|---|---|---|---|
| Material Cost (per $m^2$) | \$75 | \$5–600 | \$210–660 |
| Fabrication Cost (per $m^2$) | \$33–37 | \$33–37 | \$33–37 |
| Total Cost (per $m^2$) | \$108–112 | \$38–\$637 | \$243– \$697 |
| Conductivity | High | Moderate | Moderate-High |
| Processability (spray) | High | Moderate-low | Moderate (PANI is viscous)- High |
| Stability in water | High | Moderate | May degrade |
| Special notes | Requires waste handling | Poor dispersion | Chemical stability is limited |

electrical conductivity, increasing it from a low value of $2.215 \times 10^{-5}$ S cm$^{-1}$ for the pristine PAI membrane to an impressive $5.6 \times 10^{4}$ S cm$^{-1}$ for the Ag-PAI membrane. This substantial increase in conductivity indicates the successful integration of silver nanoparticles, establishing effective conductive pathways for electron transfer. The Nyquist plot confirmed the low resistance and high electrical conductivity of the Ag-PAI, while LSV data indicated the occurrence of ORR and HER on the membrane surface. The Ag-PAI membranes also demonstrated remarkable dye rejection rates of up to 97% for RR120 and 90% for RB at a voltage of 7 V, with only a moderate decrease in permeate flux. Additionally, the ECMs showed effective antifouling properties, achieving an FRR of 80% under a cathodic voltage of 7 V, attributed to HER and enhanced electrostatic repulsion between the foulant and the membrane surface. Additionally, the modified Ag-PAI membrane demonstrated a 55.7% inactivation rate for *E. coli*, demonstrating their potential for biofouling mitigation in wastewater filtration applications.

In summary, the highly conductive membranes developed in this study offered an effective and sustainable approach for dye removal and fouling mitigation in wastewater treatment. The membranes exhibited enhanced dye rejection, antifouling properties, antibacterial activity, and robust silver coating across various pH conditions. These features position the Ag-PAI electro-conductive membrane as a strong candidate for advanced water purification technologies. Future research will focus on optimizing membrane design for scalable production and broader commercial applications. In addition, the anti-biofouling properties of Ag-PAI electro-conductive membranes can further be studied via biofouling studies under dynamic filtration conditions.

## Supporting Information

Supporting Information is available from the Wiley Online Library or from the author.

## Acknowledgements

Z.Z. and M.Y. contributed equally to this work. The financial support for this work by the Natural Science and Engineering Research Council of Canada and Canada's Oil Sands Innovation Alliance (COSIA) is gratefully acknowledged.

## Conflict of Interest

The authors declare no conflict of interest.

## Data Availability Statement

The data that support the findings of this study are available from the corresponding author upon reasonable request.

## Keywords

antibacterial, dye removal, electro-conductive membranes, electrochemical filtration, silver-coated paiantifouling, wastewater treatment

Received: April 28, 2025
Revised: August 7, 2025
Published online:

[1] M. Dadashi Firouzjaei, E. Zolghadr, S. Ahmadalipour, N. Taghvaei, F. Akbari Afkhami, S. Nejati, M. A. Elliott, *Environ. Chem. Lett.* **2021**, *20*, 661.
[2] H. C. Flemming, *Water Res.* **2020**, *173*, 115576.
[3] S. Shao, Y. Wang, D. Shi, X. Zhang, C. Y. Tang, Z. Liu, J. Li, *Sci. Total Environ.* **2018**, *644*, 306
[4] S. Liu, H. Jiang, Y. Li, *Chem. Eng. J.* **2023**, *467*, 143456.
[5] M. M. H. Mizan, M. Rastgar, H. Sultana, P. Karami, M. Sadrzadeh, *J. Membr. Sci.* **2024**, *702*, 122806.
[6] S. Mohammad Nejad, S. F. Seyedpour, S. Aghapour Aktij, M. Dadashi Firouzjaei, M. Elliott, A. Tiraferri, M. Sadrzadeh, A. Rahimpour, *Materials Today Chemistry* **2022**, *24*, 100909
[7] M. Yassari, A. Shakeri, P. Karami, M. Sadrzadeh, *Industrial and Engineering Chemistry Research* **2024**, *63*, 566.
[8] Z. Sun, F. Dong, Q. Wu, Y. Tang, Y. Zhu, C. Gao, L. Xue, *Journal of Water Process Engineering* **2020**, *36*, 101355.
[9] Z. Sun, L. Li, Q. Wu, Z. Zhang, L. Yang, G. Jiang, C. Gao, L. Xue, *J. Membr. Sci.* **2022**, *656*, 20609.
[10] S. P. Nunes, A. R. Behzad, B. Hooghan, R. Sougrat, M. Karunakaran, N. Pradeep, U. Vainio, K.-V. Peinemann, *ACS Nano* **2011**, *5*, 3516.
[11] L. Zhu, H. Song, G. Wang, Z. Zeng, Q. Xue, *J. Membr. Sci.* **2018**, *549*, 515.
[12] Z. Salahshoor, A. Shahbazi, S. Maddah, *Chemosphere* **2021**, *278*, 130379.
[13] J. Huang, J. Luo, X. Chen, S. Feng, Y. Wan, *Environ. Sci.: Nano* **2022**, *9*, 2906.
[14] R. Tabassian, J.-H. Oh, S. Kim, D. Kim, S. Ryu, S.-M. Cho, N. Koratkar, I. Oh, *Nat. Commun.* **2016**, *7*, 13345.
[15] L. Jiang, M. Rastgar, C. Wang, S. Ke, L. He, X. Chen, Y. Song, C. He, J. Wang, M. Sadrzadeh, *Sep. Purif. Technol.* **2022**, *303*, 122274.
[16] M. Han, Y. Wang, J. Yao, C. Liu, J. W. Chew, Y. Wang, Y. Dong, L. Han, *Desalination* **2021**, *516*, 115199.
[17] H. Shao, Y. Diao, F. Zhang, S. Qin, *Desalination* **2023**, *565*, 116847.
[18] A. Karkooti, M. Rastgar, N. Nazemifard, M. Sadrzadeh, *Sci. Total Environ.* **2020**, *704*, 135365.
[19] A. Karkooti, M. Rastgar, N. Nazemifard, M. Sadrzadeh, *Sci. Total Environ.* **2020**, *704*, 135365.
[20] M. Rastgar, A. Bozorg, A. Shakeri, M. Sadrzadeh, *Chem. Eng. Res. Des.* **2019**, *141*, 413.
[21] P. Formoso, E. Pantuso, G. De Filpo, F. Nicoletta, *Membranes* **2017**, *7*, 39.
[22] L. L. Xu, Y. Xu, L. Liu, K. P. Wang, D. A. Patterson, J. Wang, *J. Membr. Sci.* **2019**, *572*, 442.
[23] G. Yi, L. Du, G. Wei, H. Zhang, H. Yu, X. Quan, S. Chen, *J. Membr. Sci.* **2022**, *658*, 120719.
[24] Z. An, J. Zhu, M. Zhang, Y. Zhou, X. Su, H. Lin, F. Sun, *Chem. Eng. J.* **2023**, *470*, 144322.
[25] L. Liu, K. Li, S. Zhao, J. Wang, H. Lan, J. Wang, *J. Membr. Sci.* **2021**, *620*, 118955.
[26] Q. Zhang, C. D. Vecitis, *J. Membr. Sci.* **2014**, *459*, 143.
[27] X. Fan, H. Zhao, X. Quan, Y. Liu, S. Chen, *Water Res.* **2016**, *88*, 285.
[28] J. J. Patil, A. Jana, B. A. Getachew, D. S. Bergsman, Z. Gariepy, B. D. Smith, Z. Lu, J. C. Grossman, *J. Mater. Chem. A* **2021**, *9*, 3270.
[29] A. M. Zaky, B. P. Chaplin, *Environmental Science and Technology* **2013**, *47*, 6554.
[30] S. O. Ganiyu, E. D. Van Hullebusch, M. Cretin, G. Esposito, M. A. Oturan, *Sep. Purif. Technol.* **2015**, *156*, 891.
[31] F. R. Omi, M. Rastgar, M. Sadrzadeh, *J. Cleaner Prod.* **2022**, *356*, 131880.
[32] L. L. Xu, L. Liu, K. P. Wang, S. Y. Zhao, Q. Y. Liu, Y. Zhang, J. Wang, *J. Membr. Sci.* **2021**, *618*, 118713.
[33] Y. Xu, Y. Yuan, X. Fan, M. Cui, J. Xiao, J. Du, Z. Pan, G. Feng, B. Lv, C. Song, T. Wang, *Journal of Water Process Engineering* **2020**, *38*, 101617.

[34] L. Du, X. Quan, X. Fan, G. Wei, S. Chen, *J. Membr. Sci.* **2020**, *596*, 117613.
[35] C. Cuevas, D. Kim, K. P. Katuri, P. Saikaly, S. P. Nunes, *J. Membr. Sci.* **2018**, *545*, 323.
[36] Z. Zandi, M. Rastgar, M. Mohseni, M. D. Firouzjaei, W. Dilokekunakul, B. Anasori, C. D. Vecitis, R. Keller, M. Wessling, M. Elliott, A. Rahimpour, M. Sadrzadeh, *Adv. Funct. Mater.* **2024**, *34*, 2401970.
[37] L. Qian, C. Yuan, X. Wang, H. Zhang, L. Du, G. Wei, S. Chen, *RSC Adv.* **2023**, *113*, 15872.
[38] D. Liu, X. Chen, B. Bian, Z. Lai, Y. Situ, *Frontiers in Chemistry* **2018**, *6*, 445.
[39] D. Bell, R. Sengpiel, M. Wessling, *J. Membr. Sci.* **2020**, *594*, 117397.
[40] K. P. Katuri, K. Katuri, M. S. Bettahalli Narasimha, X. Wang, G. Matar, S. Chisca, S. P. Nunes, P. Saikaly, *Adv. Mater.* **2016**, *28*, 9504.
[41] B. Khorshidi, J. Hajinasiri, G. Ma, S. Bhattacharjee, M. Sadrzadeh, *J. Membr. Sci.* **2016**, *500*, 151.
[42] B. Khorshidi, S. A. Hosseini, G. Ma, M. McGregor, M. Sadrzadeh, *Polymer* **2019**, *163*, 48.
[43] V. Kochkodan, N. Hilal, *Desalination* **2015**, *356*, 187.
[44] A. Ronen, W. Duan, I. Wheeldon, S. Walker, D. Jassby, *Environmental Science and Technology* **2015**, *49*, 12741.
[45] L. Wang, Y. Kong, Z. Zhang, G. Luo, X. Hou, A. Su, X. Yang, K. J. Wu, *Adv. Funct. Mater.* **2024**, *34*, 2407999.
[46] E. Zolghadr, M. Dadashi Firouzjaei, S. Aghapour Aktij, A. Aghaei, E. K. Wujcik, M. Sadrzadeh, A. Rahimpour, F. A. Afkhami, P. LeClair, M. Elliott, *Materials Today Chemistry* **2022**, *26*, 101044.
[47] S. F. Seyedpour, M. Dadashi Firouzjaei, A. Rahimpour, E. Zolghadr, A. Arabi Shamsabadi, P. Das, F. Akbari Afkhami, M. Sadrzadeh, A. Tiraferri, M. Elliott, *ACS Applied Materials and Interfaces* **2020**, *12*, 38285.
[48] M. S. Haider, G. N. Shao, S. M. Imran, S. S. Park, N. Abbas, M. S. Tahir, M. Hussain, W. Bae, H. T. Kim, *Mater. Sci. Eng., C* **2016**, *62*, 732.
[49] M. Pejman, M. Dadashi Firouzjaei, S. Aghapour Aktij, E. Zolghadr, P. Das, M. Elliott, M. Sadrzadeh, M. Sangermano, A. Rahimpour, A. Tiraferri, *Chem. Eng. J.* **2021**, *426*, 130704.
[50] Z. Tan, J. Gong, S. Fang, J. Li, W.-C. Cao, Z.-P. Chen, *Appl. Surf. Sci.* **2022**, *590*, 153059.
[51] M. Pejman, M. Dadashi Firouzjaei, S. Aghapour Aktij, P. Das, E. Zolghadr, H. Jafarian, A. Arabi Shamsabadi, M. Elliott, M. Sadrzadeh, M. Sangermano, A. Rahimpour, A. Tiraferri, *ACS Applied Materials and Interfaces* **2020**, *12*, 36287.
[52] M. Dadashi Firouzjaei, M. Pejman, M. S. Gh, S. A. Aktij, E. Zolghadr, A. Rahimpour, M. Sadrzadeh, A. A. Shamsabadi, A. Tiraferri, M. Elliott, *Sep. Purif. Technol.* **2022**, *282*, 119981.
[53] K. T. Huisman, M. H. Abdellah, D. S. Alvarez Sosa, F. R. Fernandes Simoes, B. Blankert, J. S. Vrouwenvelder, G. Szekely, *Desalination* **2024**, *582*, 117604.
[54] J. C. Jackson, C. H. Camargos, C. Liu, D. S. Martinez, A. J. Paula, C. A. Rezende, A. F. Faria, *Environmental Science: Water Research & Technology* **2024**, *10*, 639.
[55] M. Abazari, A. Sharafi, M. Hassan, H. R. Moghimi, S. Andalib, A. Ghaffari, *Polym. Bull.* **2024**, 14921.
[56] M. V. Liyanage, R. A. Latour, G. Chumanov, *Sens. Actuators, B* **2024**, *401*, 134990.
[57] D. Suresh, P. S. Goh, T. W. Wong, L. Zhang, A. F. Ismail, *Desalination* **2024**, *569*, 117040.
[58] S.-H. Park, S. H. Kim, S.-J. Park, S. Ryoo, K. Woo, J. S. Lee, T.-S. Kim, H.-D. Park, H. Park, Y. Park, J. Cho, J.-H. Lee, *J. Membr. Sci.* **2016**, *513*, 226.
[59] R. Bhandari, Y. H. Ma, *J. Membr. Sci.* **2009**, *334*, 50.
[60] G. Yang, X. Zhang, J. Zhu, Z. Li, D. Pan, F. Su, Y. Ji, C. Liu, C. Shen, *J. Mater. Sci. Technol.* **2025**, *220*, 320.
[61] C.-H. Lee, Y. J. Yun, H. Cho, K. S. Lee, M. Park, H. Y. Kim, D. I. Son, *J. Mater. Chem. C* **2018**, *6*, 7847.
[62] M. Sun, X. Wang, L. R. Winter, Y. Zhao, W. Ma, T. Hedtke, J. H. Kim, M. Elimelech, *Acs Es&T Engineering.* **2024**, *1*, 725.
[63] Q. Wang, Z. Tang, R. Herout, C. Liu, K. Yu, D. Lange, R. Godin, J. N. Kizhakkedathu, T. Troczynski, R. Wang, *Surfaces and Interfaces* **2024**, *45*, 103856.
[64] L. F. Dumée, L. He, P. C. King, M. L. Moing, I. Güller, M. Duke, P. D. Hodgson, S. Gray, A. J. Poole, L. Kong, *J. Membr. Sci.* **2015**, *475*, 552.
[65] T. P. M. Ferreira, N. C. Nepomuceno, E. L. G. Medeiros, E. S. Medeiros, F. C. Sampaio, J. E. Oliveira, M. P. Oliveira, L. S. Galvão, E. O. Bulhões, A. S. F. Santos, *Prog. Org. Coat.* **2019**, *133*, 19.
[66] X. Jiang, C. Y. Chuah, K. Goh, R. Wang, *J. Membr. Sci.* **2021**, *638*, 119708.
[67] L. Chen, K. Guan, W. Zhu, C. Peng, J. Wu, *RSC Adv.* **2018**, *8*, 39884.
[68] K. H. Lasisi, B. Tao, S. Shao, M. Liu, K. Zhang, *J. Membr. Sci.* **2025**, *724*, 123989.
[69] Z. Xian-qiu, **2007**, *58*, 2033.
[70] R. Bhaskaran, R. Chetty, *ACS Appl. Energy Mater.* **2024**, *7*, 390.
[71] X. Cui, S. Yang, X. Yan, J. Leng, S. Shuang, P. M. Ajayan, Z. Zhang, *Adv. Funct. Mater.* **2016**, *26*, 5708.
[72] R. Nogueira, M. Oliveira, W. Paterlini, ElsevierRFP Nogueira, MC Oliveira, WC PaterliniTalanta, **2005**, *66*, 86.
[73] H. Jiang, C. Tang, Y. Wang, L. Mao, Q. Sun, L. Zhang, H. Song, F. Huang, C. Zuo, *Appl. Surf. Sci.* **2021**, *564*, 150447.
[74] K. Jyoti, M. Baunthiyal, A. Singh, *Journal of Radiation Research and Applied Sciences* **2016**, *9*, 217.
[75] S. Ibrahim, Z. Ahmad, M. Z. Manzoor, M. Mujahid, Z. Faheem, A. Adnan, *Sci. Rep.* **2021**, *11*, 1.
[76] B. Khorshidi, T. Thundat, B. A. Fleck, M. Sadrzadeh, *RSC Adv.* **2015**, *5*, 54985.
[77] A. K. Shukla, J. Alam, M. S. Alhoshan, F. A. A. Ali, U. Mishra, A. A. Hamid, *ACS Applied Materials and Interfaces* **2021**, *13*, 28818.
[78] P. Karami, B. Khorshidi, J. B. P. Soares, M. Sadrzadeh, *ACS Applied Materials and Interfaces* **2020**, *12*, 2916.
[79] A. Ulvestad, A. Singer, J. N. Clark, H. M. Cho, J. W. Kim, R. Harder, J. Maser, Y. S. Meng, O. G. Shpyrko, *Science* **2015**, *348*, 1344.
[80] F. G. A. Dias, A. G. Veiga, A. P. A. C. P. Gomes, M. F. da Costa, M. L. M. Rocco, *Polym. Degrad. Stab.* **2022**, *195*, 109787.
[81] H. S. Yang, S.-H. Kim, A. G. Kannan, S. K. Kim, C. Park, D.-W. Kim, *Langmuir* **2016**, *32*, 3300.
[82] W. Hou, H. Guo, M. Wu, L. Wang, *ACS Nano* **2023**, *17*, 20560.
[83] X. Li, X. He, Y. Ling, Z. Bai, C. Liu, X. Liu, K. Jia, *J. Membr. Sci.* **2023**, *675*, 121539.
[84] T. A. Makhetha, R. M. Moutloali, *J. Membr. Sci.* **2021**, *618*, 118733.
[85] K. Wang, D. Hou, J. Wang, Z. Wang, B. Tian, P. Liang, *Appl. Surf. Sci.* **2018**, *450*, 57.
[86] Y. Ji, Q. An, X.-D. Weng, W.-S. Hung, K.-R. Lee, C.-J. Gao, *J. Membr. Sci.* **2018**, *548*, 559.
[87] G. Wolansky, A. Marmur, *Colloids Surf. A* **1999**, *156*, 381.
[88] L. Qiu, Y. Sun, Z. Guo, *J. Mater. Chem. A* **2020**, *8*, 16831.
[89] A. Debnath, S. Diyali, M. Das, S. J. Panda, D. Mondal, D. Dhak, C. S. Purohit, P. P. Ray, B. Biswas, *Dalton Trans.* **2023**, *52*, 8850.
[90] F. Sadeghian, S. Jahandari, A. Haddad, H. Rasekh, J. Li, *Journal of Rock Mechanics and Geotechnical Engineering* **2022**, *14*, 625.
[91] F. M. Siu, N. L. Ma, C. W. Tsang, *J. Chem. Phys.* **2001**, *114*, 7045.
[92] V. Romanov, C.-K. Siu, U. H. Verkerk, A. C. Hopkinson, K. W. M. Siu, *J. Phys. Chem. A* **2010**, *114*, 6964.
[93] K.-M. Ng, W.-K. Li, S.-K. Wo, C.-W. Tsang, N.-L. Ma, *Phys. Chem. Chem. Phys.* **2004**, *6*, 144.
[94] M. A. Halali, M. Larocque, *J. Membr. Sci.* **2021**, *627*, 119181.
[95] A. Thamilselvan, P. Manivel, V. Rajagopal, N. Nesakumar, V. Suryanarayanan, *Colloids Surf., B* **2019**, *180*, 1.

[96] Y. Xiang, M. B. Camarada, Y. Wen, H. Wu, J. Chen, M. Li, X. Liao, *Electrochim. Acta* **2018**, *282*, 490.
[97] Q. Y. Li, Z. F. Cui, D. S. Pepper, *Chem. Eng. J.* **1997**, *67*, 71.
[98] M. M. Meighan, M. W. Keebaugh, A. M. Quihuis, S. M. Kenyon, M. A. Hayes, *Electrophoresis* **2009**, *30*, 3786.
[99] V. D. Jetani, V. R. Shah, K. T. Patel, U. Upadhyay, *International Journal of Pharmaceutical Research and Applications* **2022**, *7*, 248.
[100] H. Zhang, X. Quan, X. Fan, G. Yi, S. Chen, H. Yu, Y. Chen, *Environmental Science and Technology* **2019**, *53*, 868.
[101] J. Zheng, Y. Li, D. Xu, R. Zhao, Y. Liu, G. Li, Q. Gao, X. Zhang, A. Volodine, B. Van der Bruggen, *Sep. Purif. Technol.* **2022**, *282*, 120155.
[102] X. Wei, S. Wang, Y. Shi, H. Xiang, J. Chen, *Industrial and Engineering Chemistry Research* **2014**, *53*, 14036.
[103] W. Yu, Y. Liu, Y. Xu, R. Li, J. Chen, B.-Q. Liao, L. Shen, H. Lin, *J. Membr. Sci.* **2019**, *581*, 401.
[104] T. H. J. A. Sleutels, A. Ter Heijne, C. J. N. Buisman, H. V. M. Hamelers, *ChemSusChem* **2012**, *5*, 1012.
[105] Y. Wang, J. Wang, Y. Ding, S. Zhou, F. Liu, *J. Membr. Sci.* **2021**, *621*, 119005.
[106] J. H. Li, X. S. Shao, Q. Zhou, M. Z. Li, Q. Q. Zhang, *Appl. Surf. Sci.* **2013**, *265*, 663.
[107] N. Bashir, M. Afzaal, A. L. Khan, R. Nawaz, A. Irfan, K. S. Almaary, F. Dabiellil, M. Bourhia, Z. Ahmed, *Sci. Rep.* **2025**, *15*, 1001.
[108] A. M. F. Linhares, C. P. Borges, F. V. Fonseca, *Polymers* **2020**, *12*, 1686.
[109] G. S. Prihandana, T. Sriani, A. D. Muthi'ah, A. Machmudah, M. Mahardika, N. Miki, *Nanomaterials* **2022**, *12*, 388.
[110] S. Agnihotri, S. Mukherji, S. Mukherji, *RSC Adv.* **2013**, *4*, 3974.
[111] A. Mollahosseini, A. Rahimpour, M. Jahamshahi, M. Peyravi, M. Khavarpour, *Desalination* **2012**, *306*, 41.
[112] J. Wang, J. Li, G. Guo, Q. Wang, J. Tang, Y. Zhao, H. Qin, T. Wahafu, H. Shen, X. Liu, X. Zhang, *Sci. Rep.* **2016**, *6*, 32699.
[113] D. Santo, J. D. Castro, Z. Benzarti, S. Cruz, A. P. Carvalho, A. Cavaleiro, S. Carvalho, *Surf. Coat. Technol.* **2024**, *487*, 130988.
[114] T. Luukkonen, J. Yliniemi, H. Sreenivasan, K. Ohenoja, M. Finnilä, G. Franchin, P. Colombo, *Sci. Rep.* **2020**, *10*, 1.
[115] Y. Bi, B. Han, S. Zimmerman, F. Perreault, S. Sinha, P. Westerhoff, *Water Res.* **2018**, *143*, 77.
[116] X. Bi, Q. Bai, M. Liang, D. Yang, S. Li, L. Wang, J. Liu, W. W. Yu, N. Sui, Z. Zhu, *Small* **2022**, *18*, 2104160.
[117] G. Wyszogrodzka, B. Marszalek, B. Gil, P. Dorozynski, *Drug Discovery Today* **2016**, *21*, 1009.
[118] Q. Yu, Z. Wu, H. Chen, *Acta Biomater.* **2015**, *16*, 1.
[119] X. Chen, J. Gao, Y. Song, Y. Gong, M. Qi, R. Hao, *Coatings* **2021**, *11*, 1548.
[120] Y. Zhang, W. Yu, R. Li, Y. Xu, L. Shen, H. Lin, B. Q. Liao, G. Wu, *Sep. Purif. Technol.* **2019**, *211*, 368.
[121] X. Wang, Z. Zhang, W. Deng, H. Xiao, L. Xia, L. Wu, *Journal of Water Process Engineering* **2025**, *72*, 107379.
[122] L. L. Xu, K. P. Wang, K. L. Li, S. Y. Zhao, J. Wang, *Sep. Purif. Technol.* **2022**, *282*, 120112.
[123] J. Huang, Z. Wang, J. Zhang, X. Zhang, J. Ma, Z. Wu, *Sci. Rep.* **2015**, *5*, 9268.
[124] X. Wang, H. Zhang, X. Wang, S. Chen, H. Yu, X. Quan, *Frontiers of Environmental Science and Engineering* **2023**, *17*, 1.
[125] S. Qi, A. D. Grossman, A. Ronen, R. Bernstein, *J. Membr. Sci.* **2022**, *662*, 120960.
[126] S. F. Anis, B. S. Lalia, A. Lesimple, R. Hashaikeh, N. Hilal, *Chem. Eng. J.* **2022**, *428*, 131184.
[127] K. Wang, L. Xu, K. Li, L. Liu, Y. Zhang, J. Wang, *J. Membr. Sci.* **2019**, *570*, 371.
[128] A. R. Moghaddam, Z. Ranjbar, *Handbook of Carbon Nanotubes* **2022**, 1773.
[129] S. Wang, Z. Tan, Y. Li, L. Sun, T. Zhang, *Thermochim. Acta* **2006**, *441*, 191.
[130] D. Rogala-Wielgus, B. Majkowska-Marzec, A. Zielinski, *Mater. Today Commun.* **2024**, *38*, 107712
[131] Alibaba, https://www.alibaba.com/product-detail/SOLVAY-Torlon-PAI-4000T-LV-4000T_1601140841014.html.
[132] Alibaba, https://www.alibaba.com/product-detail/Multi-Walled-Carbon-Nanotubes-99-for_1600565816047.html.
[133] thermoscientific, https://www.fishersci.ca/shop/products/polyaniline-emeraldine-salt-p-toluenesulfonic-acid-thermo-scientific/p-7058965.
[134] Alibaba, https://www.alibaba.com/product-detail/Single-Layer-Mxene-Titanium-Carbide-MXene_1600766772866.html.
[135] NovaCentrix, https://novacentrix.com/product/spi-529-silver-nanoparticles/.
[136] Sigma–Aldrich, https://www.sigmaaldrich.com/US/en/product/mm/109634.
[137] Sigma–Aldrich, https://www.sigmaaldrich.com/CA/en/product/sial/271012.